

# Stellar-mass black holes in young massive and open stellar clusters – VII. Comparisons with gravitational-wave events until LVK-O4a and Gaia compact binaries

Sambaran Banerjee<sup>1,\*</sup>

<sup>1</sup>Helmholtz-Instituts für Strahlen- und Kernphysik (HISKP), Nussallee 14-16, D-53115 Bonn, Germany

(Dated: February 11, 2026)

Gravitational-wave (GW) detections from the LIGO–Virgo–KAGRA (LVK) GW observatories suggest multiple formation channels contributing to the GW coalescence of compact binaries in the Universe. In this study, I assess the contribution of young massive clusters (YMC) evolving into old open clusters (OC) – the YMC/OC channel – to the GW merger population. To that end, a homogeneous grid of 90 N-body evolutionary model star clusters, spanning initial masses of  $10^4 M_{\odot} \leq M_{\text{cl}}(0) \leq 10^5 M_{\odot}$ , half-mass radii of 1–3 pc, and metallicities between 0.0002–0.02 is computed with the direct, star-by-star, post-Newtonian N-body code **NBODY7**. The N-body simulations include primordial binaries, delayed stellar remnant masses forming stellar-remnant black holes (BH) and neutron stars (NS), BH spin prescriptions, and general-relativistic recoil kicks. The model clusters are evolved until they lose most of the retained BHs. The majority of the GW mergers from the cluster models are dynamically assembled binary black holes (BBH) that merge within their host clusters, while the rarer escaped mergers are commonly primordially paired. Merger mass ratios reach down to 0.1–0.2 despite an overall bias toward nearly symmetric pairs of  $q \approx 0.8$ . The GW merger efficiency varies non-monotonically with cluster mass, peaking around  $M_{\text{cl}}(0) = 7.5 \times 10^4 M_{\odot}$  and also for  $M_{\text{cl}}(0) \leq 3.0 \times 10^4 M_{\odot}$ . The computed mergers reproduce some of the key features of the latest observed GW event catalogue, including asymmetric low-mass mergers, misaligned events among highly spinning, massive BHs, and an excess of  $30 M_{\odot}$  primaries, though they underproduce  $10 M_{\odot}$  primaries, hinting at contributions from other channels. The merger rate density from the model grid at redshift  $z = 0.2$  accounts for a quarter to a third of the observed rate depending on cosmic metallicity evolution; it increases with redshift somewhat more steeply than the cosmic star formation rate, and consistently with the overall growth of the LVK-inferred merger rate. Some of the apparent low-redshift features of the observed BBH mergers’ effective spin distribution, *e.g.*, the positive asymmetry at  $z = 0$  and the broadening with redshift, are also qualitatively reproduced. The model clusters also yield field BH- and NS-main sequence star binaries with parameters consistent with the Gaia-discovered candidates.

## I. INTRODUCTION

The known collection of general-relativistic (hereafter GR) compact binary coalescence events in the Universe, as detected in gravitational waves (hereafter GW), has undergone a major expansion after the LIGO–Virgo–KAGRA (hereafter LVK; Ref. [1]) collaboration has just updated their gravitational wave transient catalogue (hereafter GWTC) with the GW-event candidates from the first half of their fourth observing run, ‘O4a’ [2]. The current GWTC contains  $\approx 166$  events that are designated to be astrophysical GW events (having  $p_{\text{astro}} > 0.5$ )<sup>1</sup>. Like the previous GW-event catalogues, the vast majority of the to-date-observed GW events remain classified as binary stellar-remnant black hole (hereafter BBH) GW mergers. A range of scenarios have been proposed as potential formation channels for BBH mergers; see Refs. [3, 4] for comprehensive reviews. Such scenarios include dynamical interactions among stellar-remnant black holes (hereafter BH) in dense star clusters [5–7], isolated evolution of massive-stellar binaries (*e.g.*, [8]), interacting BHs in AGN gas disks (*e.g.*, [9, 10]), isolated

evolution of hierarchical massive-stellar systems (*e.g.*, a massive field triple-star; [11, 12]), close flyby interactions involving BBHs in the galactic field (*e.g.*, [13]), and cluster and galactic tides on wide BBHs (*e.g.*, [14, 15]). The properties of the observed GW events and of their population would, in turn, serve to constrain the formation channels, their physics, and the physics of stellar remnant formation.

Indeed, underlying population properties, especially the rather complex, multi-peaked merger primary mass distribution and the asymmetric effective spin distribution, as inferred from the latest ensemble of observed GW events, suggest formation of these events via a range of mechanisms (or formation channels), rather than through a single dominant channel (*e.g.*, Refs. [16–18]). In particular, the latest inferred population distributions point to both the importance of dynamical interactions (*i.e.*, the ‘dynamical channel’) and isolated binary evolution (*i.e.*, the ‘isolated-binary channel’) in forming GW sources [17]. Therefore, to obtain an understanding of the underlying distributions of GW events in the Universe and to avoid misleading interpretations, it is nevertheless crucial to explore individual formation channels thoroughly. A relatively newly conceived but widely discussed channel is GW merger formation in young massive clusters (hereafter YMC) and moderately massive open clusters (hereafter OC) [19–22]. Observed YMCs in the

\* banerjee@hiskp.uni-bonn.de; sambaran.banerjee@gmail.com

<sup>1</sup> <https://gwosc.org/eventapi/html/GWTC/>

Milky Way (hereafter MW) and local group (hereafter LG) galaxies are typically of  $\sim 10^4 M_\odot$  and parsecs scale length [23, 24], and through dynamical and stellar evolution, they would evolve into moderate mass, extended OCs. While more massive globular clusters (typically of  $\sim 10^5 M_\odot$ ; hereafter GC) are canonically considered as the most prominent source of dynamically assembled BBH mergers [25, 26], YMCs and OCs, owing to their much shorter relaxation time, low velocity dispersion, shorter lifespan, and possibly different cosmic formation history, comprise a separate formation channel by their own right [27–30]. See also Ref. [31] (their Secs. I and IV) for additional discussions on the physics of star cluster evolution in the presence of a subpopulation comprising of retained BHs and neutron stars (hereafter NS). For brevity, this discussion is skipped in this paper.

In this study, this YMC/OC channel of GW source formation is revisited based on a newly computed grid comprising long-term evolutionary models of  $10^4 - 10^5 M_\odot$ , pc-scale star clusters. The details of the grid are presented in Sec. II. Evolutionary model grids in the YMC/OC regime producing populations of GW mergers have previously been explored by several groups and authors. Ref. [32] presented a set of  $\approx 70$  long-term (evolution time of several to 10 Gyr) direct N-body evolution (see Sec. II B) of model star clusters, of initial masses ranging over  $10^4 M_\odot - 10^5 M_\odot$ . Ref. [33] explored a grid of 40 massive (membership  $\sim 10^5$ ) clusters that were evolved for  $\approx 300$  Myr with direct N-body integration. Ref. [34] presented a grid of 32 particle-particle-particle-Tree (or ‘P3Tree’) N-body evolutionary model clusters [35] with initial masses and (half-mass) densities ranging over  $10^4 - 10^5 M_\odot$  and  $10^3 - 10^5 M_\odot \text{pc}^{-3}$ , which were typically evolved up to 1 Gyr (three models were evolved up to 3 Gyr). These authors have additionally evolved two cluster models of initially  $10^6 M_\odot$  for up to  $\approx 600$  Myr. Based on a suite of 95 long-term (until 10 Gyr or dissolution) direct N-body simulations of initially  $3 \times 10^4 M_\odot$  clusters spanning across a wide range of galactocentric distances (or external tidal field), Ref. [31] addressed the impact of galactic tidal field on the production of GW sources from YMC/OCs.

Apart from YMC/OC-type clusters, evolutionary grids have been computed for models representing GCs, with a focus on GW source formation in them. Ref. [36] presented a grid of 148 GC models with masses within  $10^5 M_\odot - 10^6 M_\odot$ , which were evolved for 12 Gyr via a Monte Carlo approach. Ref. [37] presented similar (but more numerous; 2000 models) Monte Carlo GC model grids, that were evolved up to a similar extent. Ref. [38] evolved 19 GC-like model clusters that are initially of  $0.7 - 5.9 \times 10^5 M_\odot$  and extremely dense ( $10^4 - 10^7 M_\odot \text{pc}^{-3}$ ). With direct N-body integration, they evolved the clusters up to  $\lesssim 2.4$  Gyr. On the other hand, by applying direct N-body integration, Refs. [28, 39, 40] presented extensive sets of evolutionary models of low mass ( $10^2 - 10^4 M_\odot$ ) star clusters. See Fig. 1 of Ref. [38] for a comprehensive overview of the model cluster suits

from various authors.

Clearly, there exists a dearth of long-term evolutionary model grids of star clusters that initiate at a mass within  $10^4 - 10^5 M_\odot$ . On one hand, this YMC/OC mass range is highly relevant from the astrophysics point of view, as it bridges low-mass star clusters to massive GCs. On the other hand, a star cluster in this mass range is probably most tedious to deal with when it comes to computing its evolution: it is not populous enough to be treated with fast analytical [41, 42] or statistical (*e.g.*, Monte Carlo [43, 44]) approaches, but it is rather too populous to be evolved until late dynamical ages with direct N-body integration, even with the latest hardware. See Ref. [31] for further discussions. Consequently, over this mass range, star cluster model grids in the literature have so far turned out to be short-term evolved, sparse, or heterogeneous.

This study attempts to address this deficit by presenting a new evolutionary grid of  $90 10^4 - 10^5 M_\odot$  model star clusters that is homogeneous in the clusters’ initial and physical properties, and the clusters are evolved at least until most of the BHs are depleted from them. Furthermore, the GW merger population from this grid is compared with the latest GWTC and its inferred population distributions [2, 17]. A complete processing of the clusters’ BHs makes such a comparison complete and reliable. Since it is likely that the observed event population is an outcome of multiple formation channels (see above), the author does not aim to reproduce the observed population based on the GW mergers from the model clusters. Rather, the objective here is to see to what extent the YMC/OC channel contributes to the observed event population.

This paper is organised as follows. Sec. II describes the computed N-body star cluster model grid. Sec. III describes the results of the N-body simulations: Sec. III A discusses the general long-term evolution of the model clusters and Sec. III B describes the GW mergers formed from them. Sec. IV compares the model mergers with GWTC: Sec. IV A compares the model-merger population properties with LVK’s GWTC-based population properties and Sec. IV B discusses the evolution of the properties with redshift. Sec. V discusses the formation of field compact-star–normal-star binaries from the model cluster grid and compares the model binaries with observed Gaia BH-MS and NS-MS binary candidates. Sec. VI summarises the results, discusses the current limitations, and suggests potential improvements.

## II. MODELLING STAR CLUSTER EVOLUTION

This section describes the newly computed grid of evolutionary models of star clusters.

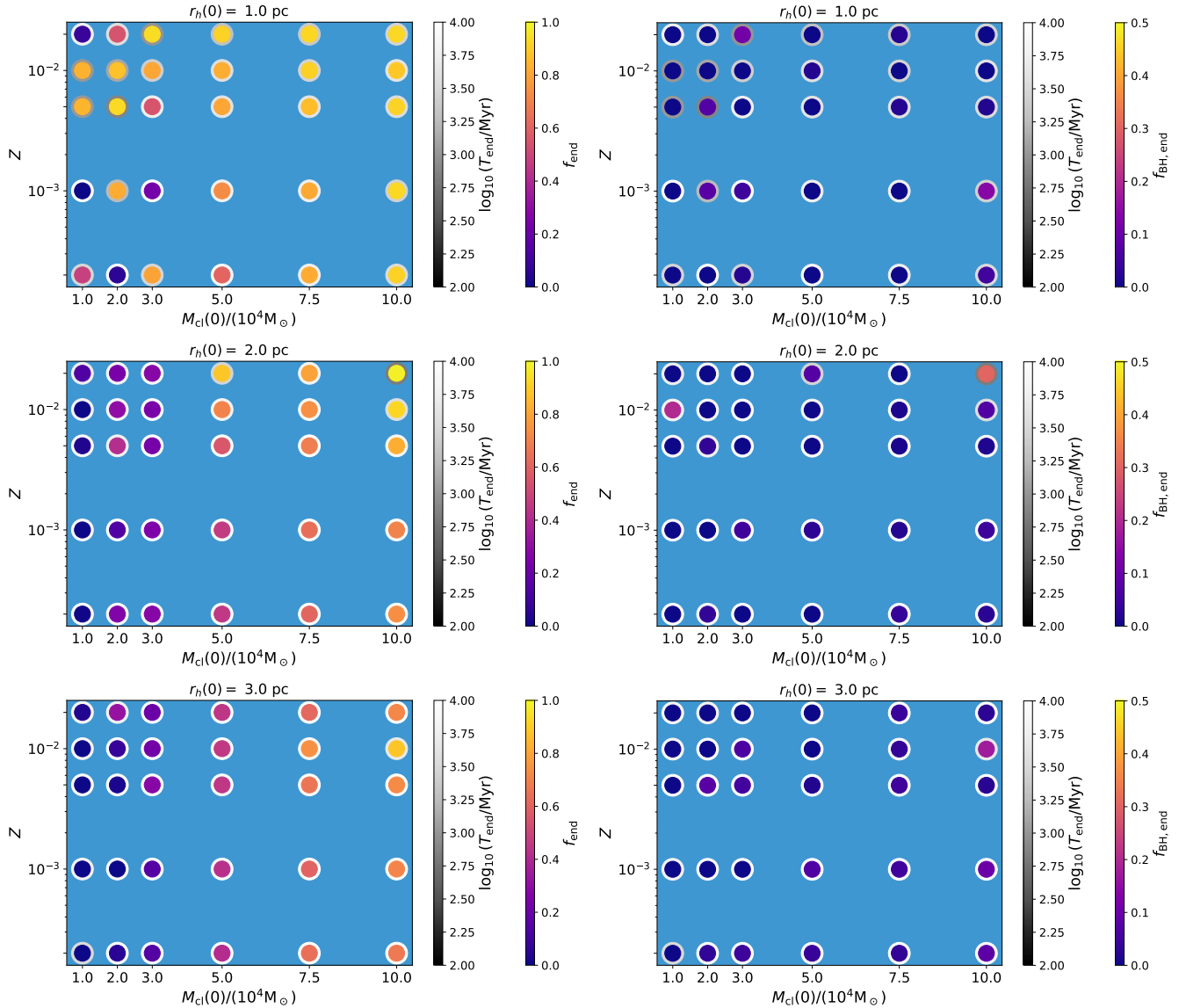


FIG. 1. Depiction of the computed grid of 90 evolutionary model star clusters spanning across ranges of cluster initial mass,  $M_{\text{cl}}(0)$ , initial half-mass radius,  $r_h(0)$ , and metallicity,  $Z$ . The panels in the upper, middle, and lower rows correspond to the computed grid points (filled circles) for the clusters with  $r_h(0) = 1$ , 2, and 3 pc, respectively. The greyscale color coding of the edge of a circle represents the end time in Myr,  $T_{\text{end}}$ , of the corresponding N-body simulation. The circles' fill colour in the left column represents  $f_{\text{end}}$ , which is the number of bound cluster members at the end of the simulation relative to the initial cluster membership. The circles' fill colour in the right column represents  $f_{\text{BH},\text{end}}$ , which is the number of BHs bound to the cluster at the end of the simulation relative to the peak BH membership of the cluster during its evolution. See Table. III (Appendix A) for more details.

### A. The star cluster model grid

In this study, a grid of star cluster models of initial masses ranging over  $10^4 M_{\odot} \leq M_{\text{cl}}(0) \leq 10^5 M_{\odot}$  is evolved. The initial density and velocity dispersion profiles of the clusters are taken to be according to the Plummer model [45, 46]. The initial models have masses of  $M_{\text{cl}}(0) = 10^4 M_{\odot}$ ,  $2 \times 10^4 M_{\odot}$ ,  $3 \times 10^4 M_{\odot}$ ,  $5 \times 10^4 M_{\odot}$ ,  $7.5 \times 10^4 M_{\odot}$ , and  $10^5 M_{\odot}$ , and half-mass radii of  $r_h(0) = 1$  pc, 2 pc, and 3 pc. Each model cluster is evolved for the

metallicities  $Z = 0.0002$ , 0.001, 0.005, 0.01, and 0.02. These initial conditions together comprise a grid of 90 evolutionary star cluster models covering wide ranges of  $M_{\text{cl}}(0)$ ,  $r_h(0)$ , and  $Z$ . The computed grid is depicted in Fig. 1.

During its evolution, each model cluster is subjected to a solar-neighbourhood-like external galactic field by placing the cluster on a circular orbit at a MW galactocentric distance of  $r_g = 8.5$  kpc. The MW tidal field is modelled based on an axisymmetric bulge-disk-halo potential as

in Ref. [31]. That reference has investigated the impact of galactic tidal field on GW production from clusters, and has shown that the variation of external field would only have a moderate impact on GW production, for the cluster mass range considered here. Therefore, the current model grid complementarily focusses on variation in  $M_{\text{cl}}(0)$ ,  $r_{\text{h}}(0)$ , and  $Z$ , which would allow for constructing a model cluster population that incorporates a critical aspect when it comes to physics of star clusters, namely, the cluster's mass. In contrast, the model grid of Ref. [31] varied  $r_g$ ,  $r_{\text{h}}(0)$ , and  $Z$ .

## B. Direct, star-by-star, post-Newtonian N-body simulations

Each initial model in the above-described grid is evolved with the star-by-star, direct, post-Newtonian (hereafter PN) N-body code **NBODY7** [20]. The code integrates the orbit of each member subject to the combined gravitational field of the rest of the members plus any external gravitational field. The main orbit integrations are carried out by a fourth-order Hermite integrator. To tackle the time-stepping and stalling issues during close approaches among the members [47], the code does not implement any force-softening or another approximate procedure. Instead, it applies the much more accurate KS- and Chain-regularisation techniques. The integration is forwarded with individual, grouped time stepping for all members. The details of all algorithms employed in **NBODY7** can be found in Ref. [48]. In this work, an updated version of **NBODY7** as described in Refs. [49] and [32] is used. These updates include implementations of more recent stellar wind mass loss and remnant-formation prescriptions, and also implementations of numerical relativity (hereafter NR)-based GR merger recoil and tracking of spins of higher-generation BHs inside the cluster, at runtime.

Runtime stellar and binary evolution is achieved in **NBODY7** through its coupling with the rapid, analytical binary evolution code **BSE** [50, 51]. Runtime PN evolution of compact binaries and higher order systems is computed by incorporating the few-body integrator **ARCHAIN** [52, 53]. In the present computations, the ‘delayed’ remnant-mass model along with the possibility of occurrence of pair-instability supernova (hereafter PSN) and pulsation-pair-instability supernova (hereafter PPSN) are chosen [49, 54, 55]. The delayed remnant-mass prescription allows the formation of stellar remnants within the so-called ‘lower mass gap’ between  $2M_{\odot} - 5M_{\odot}$ ; in other words, no lower mass gap exists for the chosen delayed remnant-mass prescription. This choice is consistent with the observations of GW-merger candidates involving such lower-mass-gap compact objects [56, 57]. In the present simulations, the canonical  $2.5M_{\odot}$  upper limit for NS mass [55] is adopted. Due to allowing PPSN and PSN, the mass spectrum of BHs derived from single stars and non-interacting binary

members evolving from zero age main sequence exhibits the conventional PSN mass gap over  $\approx 40M_{\odot} - 120M_{\odot}$  [58, 59] (but see below).

A newly formed NS or BH is assigned a random supernova (hereafter SN) natal kick velocity, whose base magnitude is drawn from a Maxwellian distribution of dispersion  $\sigma = 265 \text{ km s}^{-1}$ . This kick magnitude is then moderated based on the SN mass fallback fraction [54] and linear momentum conservation, as in Ref. [49]. Typically, this would cause retention of the  $\gtrsim 8M_{\odot}$  BHs at birth, inside the present model clusters. All lower mass BHs and core-collapse-SN-formed NSs escape the cluster at formation due to their higher natal kick. However, NSs formed via electron capture supernovae (hereafter ECS) receive small natal kicks [60] and are typically retained in the cluster at their formation.

The stars in the initial models are taken to be at the zero age main sequence (hereafter ZAMS) and of masses between  $0.08M_{\odot} \leq m_* \leq 150.0M_{\odot}$ , which are distributed according to the Kroupa initial mass function (hereafter IMF) [61]. In all initial models, the stars have an overall (see below) primordial-binary fraction of  $f_{\text{bin}} = 10\%$ . However, the initial binary fraction of the O-type stars ( $m_* \geq 16.0M_{\odot}$ ), which are initially paired only among themselves, is taken to be  $f_{\text{Obin}}(0) = 100\%$ , which is consistent with the observed high binary fraction among O-stars in young clusters and associations [62–64]. The O-star binaries initially follow the observed orbital-period distribution of Ref. [62] and a uniform mass-ratio distribution. The initial orbital periods of the non-O-star primordial binaries follow the period distribution of Ref. [65] and their mass-ratio distribution is also uniform. The initial eccentricity of the O-star binaries follows the distribution of Ref. [62] and that of the rest of the binaries follows the thermal eccentricity distribution [66]. As explained in Ref. [67], such a scheme for primordial binaries provides a reasonable compromise between the economy of computing and consistencies with observations.

In the present models, small birth spins, as per the ‘MESA’ BH-spin model of Ref. [68], are assigned to all BHs derived from single stars or from members of non-mass-transferring or non-interacting binaries. Such small spin magnitudes correspond to a Kerr parameter (dimensionless spin) of  $0.05 \lesssim a \lesssim 0.15$ , and are caused by dynamo-driven efficient core-to-envelope angular momentum transport in the pre-SN BH progenitor star [69, 70]. See Appendix C for further details.

In the event of a BH-star merger (the formation of a BH Thorne–Zytkow object or BH-TZO [71]) during a simulation,  $f_{\text{TZ}} = 95\%$  of the merging star’s mass is assumed to be accreted onto the BH. In runtime star-star collisions, a merged star is formed where an equivalent of  $f_{\text{mrg}} = 20\%$  of the secondary’s mass is assumed to be lost in the merger process [72, 73]. The merged star is rejuvenated according to the recipes implemented in **BSE** [51] that assume complete mixing. Notably, the extent of mass accretion onto a BH and mass loss in star-star mergers are ambiguous. The above choices favour the

formation of massive BHs, especially those within the canonical PSN mass gap between  $\approx 40M_{\odot} - 120M_{\odot}$ , even in moderately dense environments. As demonstrated in Ref. [33], that way the extent of massive BH formation in star clusters is consistent with the BBH merger rate in the PSN gap as observed by LVK [74, 75]. Besides, an optimistic formation of massive BHs would ultimately allow constraining their production through population modelling.

The author aimed to evolve each model cluster at least until most of the BHs that were retained in the cluster at their birth are depleted due to dynamical ejections and GW-merger recoils. Fig. 1 depicts the evolution times and the simulation end states (number fractions of retained BHs and total membership) for the models corresponding to each grid point. The relevant end-state values for each run are quoted in Table III (Appendix A). As seen, nearly all models are indeed evolved until the cluster is nearly deprived of BHs. After this, the cluster enters the binary-burning state, often making the run tedious to continue (see Ref. [31] and references therein for a discussion). Nevertheless, it was possible to evolve  $\approx 40$  of the model clusters beyond 10 Gyr. A handful of runs have prematurely crashed in a way that they could not be recovered for continuation.

### III. RESULTS

Table III (Appendix A) summarizes the outcomes of each model cluster. Below, the results are discussed in detail.

#### A. Star cluster evolution

Due to retention of BHs, the evolution of the model clusters is generally affected by the strong mass segregation of BHs [66], central BH core formation, and the associated balanced evolution — also termed BH-heating [19, 41, 77, 78]. For a given initial mass and size of a cluster, a cluster with lower metallicity generally produces BHs that are more massive and larger in number, due to weaker stellar winds and shorter stellar lifetimes [49]. This, in turn, would initially form a more massive and concentrated central BH core, leading to more energy release in close encounters inside the core, and causing the cluster to expand to a larger extent. The cluster expansion, in turn, serves as a ‘negative feedback’ by causing also the BH-core to expand, thereby moderating the associated dynamical ejections and depletion of the BHs [78, 79]. See Sec. I of Ref. [31] and the references therein for a comprehensive discussion on BH heating. Other initial parameters being identical, a more massive cluster would retain and dynamically process the BHs for a longer duration, leading to generally longer delay times of BBH mergers and ejections from them. On the other hand, a more concentrated cluster would process the BHs

faster. See Refs. [21, 36, 67] for detailed discussions and demonstrations of these trends. Fig. 2 (this work) comprehensively demonstrates the evolutionary trends with  $Z$ ,  $M_{\text{cl}}(0)$ , and  $r_{\text{h}}(0)$  by taking advantage of the present complete evolutionary model grid <sup>2</sup>.

If the BH-progenitor stars of a star cluster are in primordial binaries, the BHs’ birth masses can be affected by the binaries’ internal evolutionary processes (*e.g.*, mass transfer and tidal interaction between binary members) and as well by stellar collisions triggered by binary-single and binary-binary dynamical encounters. Furthermore, the internal evolution of a binary itself can be influenced by dynamical encounters. Accordingly, birth masses of the BHs (and also of the NSs) derived from a dynamically interacting massive binary population would deviate stochastically from a well-defined initial-mass–remnant-mass relation, as has been demonstrated in recent studies. In particular, star-star collision products can produce massive BHs within the canonical PSN mass gap between  $40M_{\odot} - 120M_{\odot}$  [32, 33, 49, 80–83], that would typically be unachievable by single stellar evolution beginning from the ZAMS <sup>3</sup>. To produce a BH with birth mass within this ‘forbidden’ mass range, the merger needs to take place between two massive stars with dissimilar evolutionary stages, so that a helium core of mass lower than the PPSN threshold can acquire an over-massive hydrogen envelope. Dense, dynamically active environments such as the present cluster models enable collisions and mergers among a wide range of stars, facilitating the formation of PSN-gap BHs.

Fig. 3 shows the time evolution of the total luminous mass,  $M_{\text{cl},*}$ , and size,  $r'_{\text{h},*}$  (projected half-mass radius of the luminous mass distribution), of the model clusters at low and high metallicities. These low- $Z$  (high- $Z$ ) curves are compared with the masses and sizes of the observed star clusters across ages in the SMC [76] (MW, M31, and LMC [23]). The  $Z$  values of the models presented in Fig. 3 are chosen to be similar to the metallicities of the observed clusters as stated in the corresponding references. As seen, the computed models represent certain subsets of the observed clusters. For the observed SMC sample, the computed models mainly cover the relatively massive ( $M_{\text{cl},*} \gtrsim 10^3 M_{\odot}$ ), old (age  $t \gtrsim 1$  Gyr), and moderately extended ( $2\text{pc} \lesssim r'_{\text{h},*} \lesssim 8\text{pc}$ ) clusters. While

<sup>2</sup> The lines or the boundaries in Figs. 2, 3, 10 and 11 are moderately smoothed by applying the Savitzky-Golay-Filter (with 12 points and polynomial order 3), as available in the SciPy module `scipy.signal.savgol_filter`.

<sup>3</sup> Conventionally used single stellar evolution models, including the one adopted in this work (Sec. II B), result in a PSN mass gap of stellar-remnant BHs. However, alternative (non-collision-product) single star evolution models exist that allow BH formation within the conventional PSN mass gap by either modifying/bypassing the occurrence of pair instability and pulsation pair instability (*e.g.*, Refs. [84, 85]) or modifying the stellar wind [86]. Pure isolated evolution of massive binaries may also result in PSN-gap BHs by, *e.g.*, allowing for super-Eddington accretion [87].

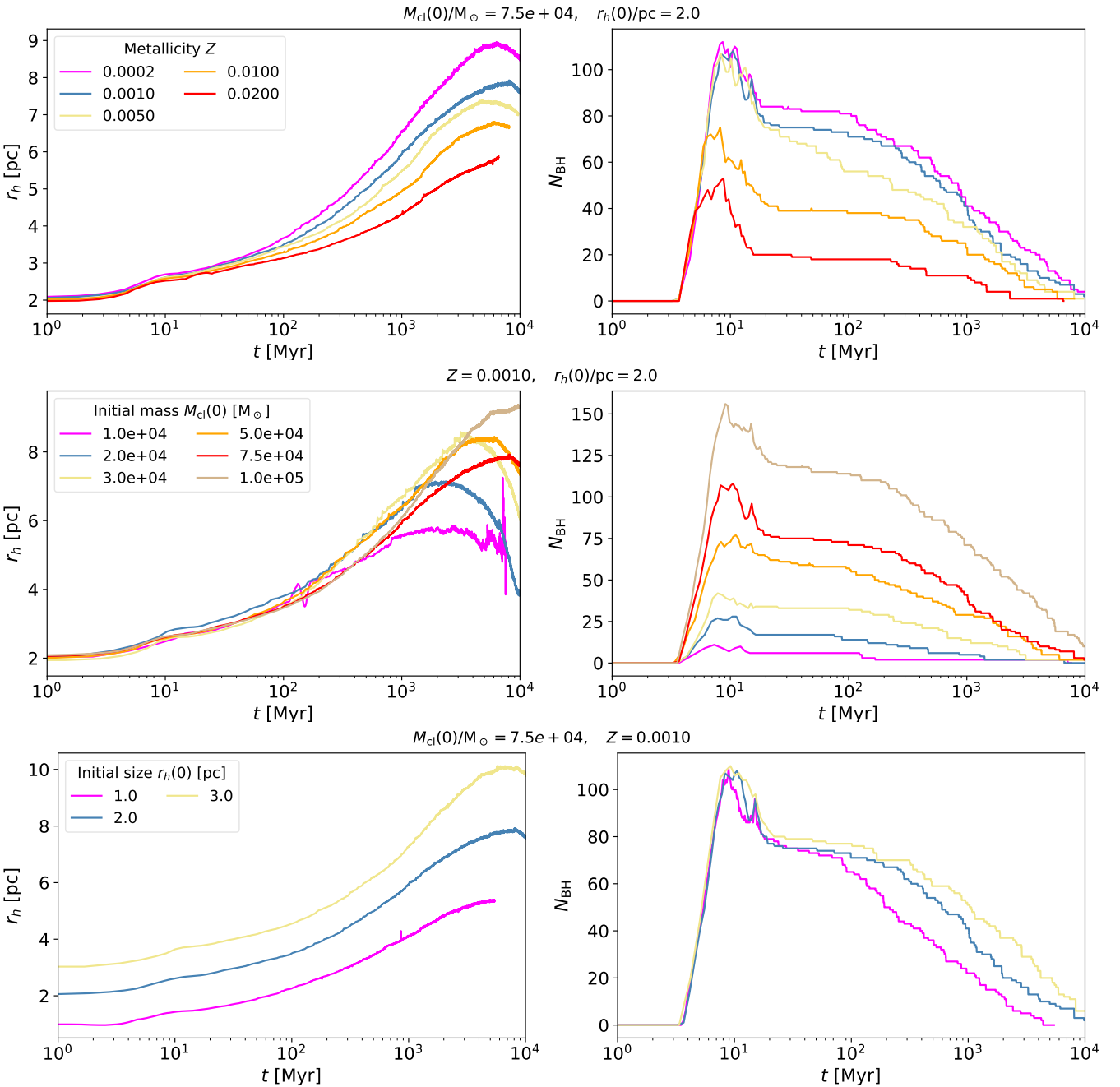


FIG. 2. Dependence of model cluster evolution with variation of cluster metallicity,  $Z$  (upper panel), initial mass,  $M_{\text{cl}}(0)$  (middle panel), and initial size,  $r_h(0)$  (lower panel). For each variation (legend), the other two grid coordinates are kept constant, as indicated in each row's title. Shown are the time evolution of the half-mass radius,  $r_h$  (left column), and the number of BHs bound to the cluster,  $N_{\text{BH}}$  (right column).

the SMC clusters' sizes are also generally covered by the model clusters at younger ages, the present model grid, by construction, does not contain any cluster over the mass range  $10^2 M_{\odot} \lesssim M_{\text{cl},*} \lesssim 10^3 M_{\odot}$  for  $t \lesssim 300$  Myr, unlike the observed sample.

For the observed MW-LMC-M31 sample, the masses are well represented by the model clusters. As for sizes, the model clusters cover up to  $r'_{h,*} \lesssim 5$  pc - the highly

extended clusters of MW, LMC, and M31 are not covered by the present grid. Notably, all observed clusters in the MW-LMC-M31 sample are massive ( $M_{\text{cl},*} \gtrsim 10^4 M_{\odot}$ ) and younger than  $\approx 100$  Myr. The above model-observation comparison should be considered as preliminary and at a ballpark level. The observed cluster samples are far from complete. Also, for a detailed comparison, synthetic observations of the model clusters are

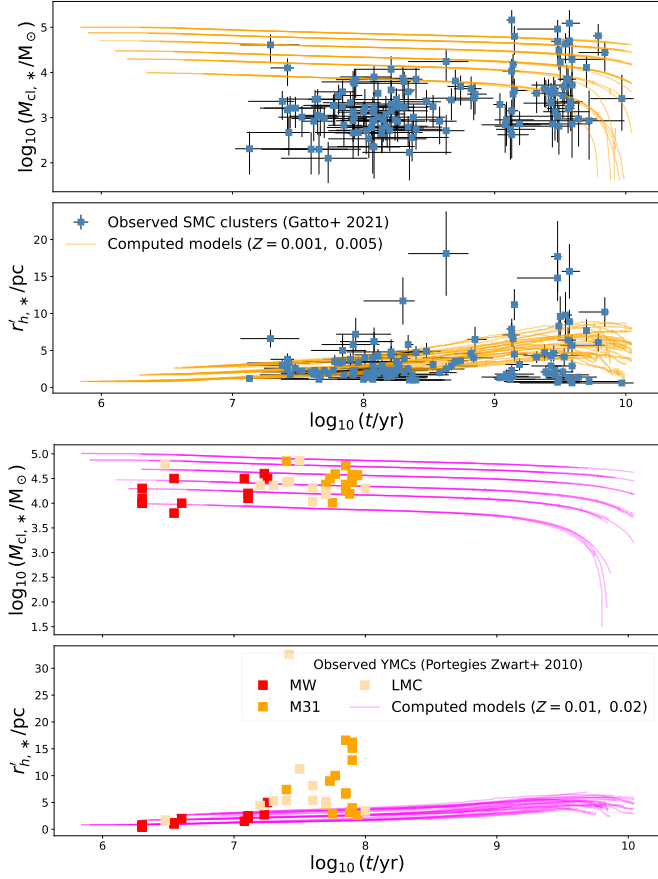


FIG. 3. Time evolution of the luminous mass (total mass of luminous stars within the instantaneous tidal radius),  $M_{\text{cl},*}$ , and size (corresponding projected half-mass radius, averaged over three orthogonal projections),  $r'_{\text{h},*}$ , of the computed model star clusters as functions of the cluster-evolutionary age,  $t$ , at low ( $Z = 0.001, 0.005$ ; upper pair of panels) and high ( $Z = 0.01, 0.02$ ; lower pair of panels) metallicities (solid lines). The masses, sizes, and ages of the low- $Z$  (high- $Z$ ) models are compared with those of the observed star clusters across ages in the SMC [76] (MW, M31, and LMC [23]) (filled symbols).

necessary, which is beyond the scope of this study. However, it can be said that the computed models are generally comparable to the observed massive and compact star clusters of the MW and Local Group galaxies across ages.

## B. Gravitational-wave mergers from model clusters

Due to the formation of a strongly mass-segregated, dense, central BH subpopulation or BH-core, these model clusters have the potential to form BBHs through close dynamical interactions, a fraction of which can undergo GW inspiral and merger. The key is to boost the BBH's eccentricity to an adequately high value via, *e.g.*, von Zeipel-Kozai-Lidov mechanism, chaotic triple

or higher-multiplicity interactions, or close flyby encounters [20, 88, 89]. The GR inspiral and merger can take place inside the cluster based on the GR coalescence criteria of Ref. [20]. Otherwise, if the BBH is dynamically ejected from the cluster, then, depending on the binary parameters at the time of the ejection [90], it may merge outside the cluster's tidal radius within the Hubble time to become a GW event candidate. Due to the presence of massive primordial binaries (Sec. II B), the pairing of compact binaries (apart from BBHs, also possibly NS-BH and NS-NS binaries) can happen also due to the evolution of the massive binaries, *i.e.*, the pair maintains the primordial-binary membership. After formation, such a primordially paired compact binary can undergo GW coalescence in-cluster or following ejection from the cluster (the ejection being due to either dynamical encounters or natal kick of the member remnants) maintaining the membership, leading to a primordially paired GW merger. However, due to the dynamical perturbations of the primordial binaries or of their derivative compact binaries inside their host clusters, their binary-evolution pathways are potentially altered. Therefore, the primordially paired merger population from star clusters does not necessarily represent compact binary GR mergers from isolated massive binary evolution.

Table I quotes the number of in-cluster and ejected GW mergers from all the 90 computed model clusters, distinguishing between dynamically and primordially paired mergers. The in-cluster mergers are primarily dynamically paired (97.3% of them), while the majority (69.0%) of the ejected mergers are primordially paired. Overall, the GW mergers from these cluster models are predominantly (79.3%) dynamically paired. Also, the majority (72.9%) of the mergers take place inside the clusters.

Fig. 4 plots the masses of all the GR mergers from the computed model grid. The left panel plots the mergers' primary mass,  $m_1$ , versus secondary mass,  $m_2$  ( $m_1 \geq m_2$ ), and the right panel plots their total mass,  $m_{\text{tot}}$ , vs mass ratio,  $q (\equiv m_2/m_1 \leq 1)$ . The symbols are colour-coded according to the mergers' parent cluster's initial half-mass density,  $\rho_{\text{cl},0}$ . See the figure's caption for the meanings of the symbols and other details. It is seen that the mergers with  $m_2 \lesssim 10M_{\odot}$  are nearly all ejected and primordially paired, whereas the more massive mergers are more numerous and predominantly in-cluster and dynamically paired. In fact, the least massive dynamically paired merger has  $m_1 \approx 10M_{\odot}$ ,  $m_2 \approx 10M_{\odot}$ .

A number of these GW mergers have one or both of the component masses within the PSN mass gap between  $\approx 40M_{\odot} - 120M_{\odot}$ . In this paper, such mergers are referred to as PSN-gap mergers. In the current cluster models, these massive BHs are mainly outcomes of star-star and BH-star collisions (Sects. II B, III A). While hierarchical GR coalescence is a rather common way to produce BHs within and beyond the PSN mass gap in massive GCs [26, 91, 92] and nuclear star clusters [93–95], this channel is disfavoured in the present, moderate-mass clusters due

TABLE I. Counts of GW coalescences from the computed model grid (Table III, Figure 1).

Merger location	Dynamically paired	Primordially paired	Total
Inside cluster	110	3	113
Ejected	13	29	42
Total	123	32	155

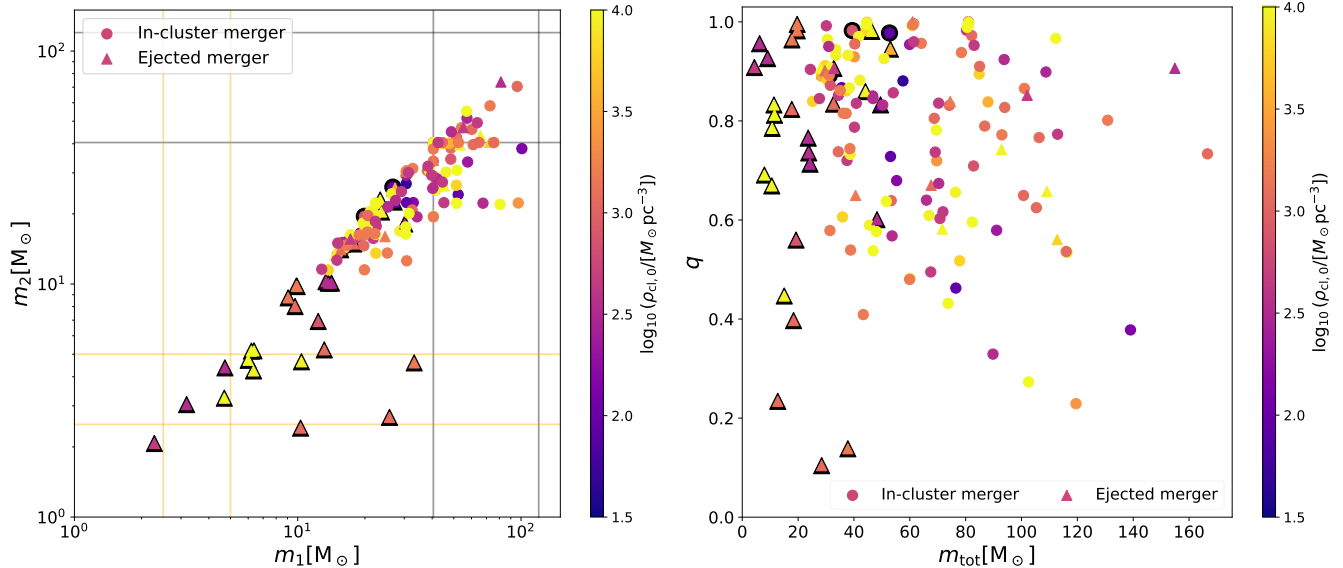


FIG. 4. Compilation of GW mergers of compact binaries produced by all the 90 evolutionary model clusters in this work. **Left panel:** the filled symbols represent the mergers' primary mass,  $m_1$ , along the X-axis versus the mergers' secondary mass,  $m_2$ , along the Y-axis ( $m_1 \geq m_2$ ). The circles and the triangles mark the in-cluster and the ejected mergers, respectively. Those merging binaries that preserve their primordial pairing (*i.e.*, the primordially paired mergers) are indicated by an additional thick-lined edge around their respective symbols. The data points are colour-coded with respect to the initial half-mass density,  $\rho_{cl,0}$ , of their respective parent cluster (colour bar). The canonical lower or NS-BH mass gap between  $2.5M_\odot - 5.0M_\odot$  and the upper or PSN mas gap between  $40.5M_\odot - 120.0M_\odot$  are marked along the axes with the horizontal and vertical lines. **Right panel:** the filled symbols represent the mergers' total mass,  $m_{\text{tot}}$ , along the X-axis versus the mergers' mass ratio,  $q \equiv m_2/m_1 \leq 1$ , along the Y-axis. The meaning of the different symbols and the colour-coding is the same as in the left panel. See text for further details.

to their lower escape speeds ( $\lesssim 50 \text{ km s}^{-1}$ ). The most massive BBH merger obtained from the present computations is of  $m_{\text{tot}} = 166.6M_\odot$ . The present event set also includes one NS-NS merger, one NS-BH merger and several mergers involving lower-mass-gap (hereafter LMG) compact objects (Sec. II B), all of which are ejected, primordially paired mergers (see Fig. 4). Due to the adopted delayed remnant mass model, LMG objects form in the model clusters simply due to the single-star remnant formation process. Due to the adopted NS upper mass limit, all LMG objects are designated as BH in these computations.

As for the mergers' mass ratio, they can extend to highly asymmetric values ( $q \ll 1$ ) although, overall, symmetric mergers ( $q \rightarrow 1$ ) are favoured. This preference arises due to the fact that both massive binary evolution and BH-core dynamical interactions tend to pair BHs of similar masses [8, 21, 96]. The lower-mass, primordially paired, escaped mergers extend to being as asymmetric as  $q \approx 0.1$  (Fig. 4), due to the NS-BH and LMG-BH

mergers. For the in-cluster, dynamically paired mergers,  $q \gtrsim 0.2$ . Overall, no clear trend between the mergers' masses and the parent clusters' initial density is found in these models (Fig. 4) – it is possible that an underlying trend is washed away due to the stochastic nature of the dynamical processes and the limited number of events.

Fig. 5 (left panel) plots the model mergers'  $m_{\text{tot}}$  against their delay time,  $t_{\text{mrg}}$ , distinguishing between in-cluster, ejected, primordially paired, and dynamically paired mergers as in Fig. 4. In this study, the delay time of a GW merger (or event) is defined as the time of the merger since the beginning of the parent model cluster's evolution. Here, the data points are colour-coded according to the events' individual inspiral time until the merger,  $\tau_{\text{insp}}$ ; see the figure's caption for more details. For in-cluster mergers, the  $\tau_{\text{insp}}$  values are obtained from the compact binary's orbit-averaged orbital decay due to gravitational radiation [90], beginning from the state when the in-spiralling binary can be considered to be dynamically decoupled from the rest of the cluster [20]. The

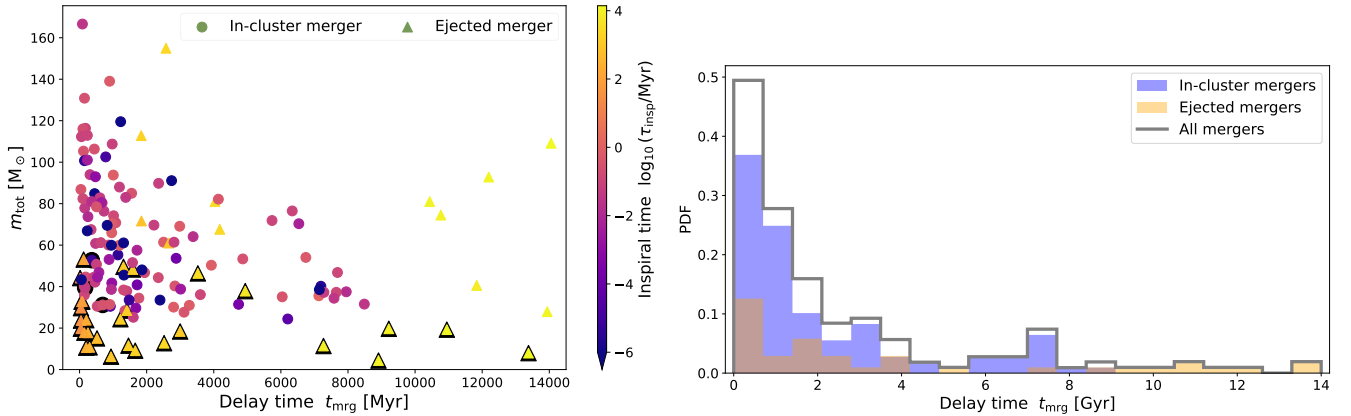


FIG. 5. **Left panel:** the filled symbols mark the delay times,  $t_{\text{mrg}}$  (X-axis), of all compact binary mergers from the model-cluster grid versus their corresponding total mass,  $m_{\text{tot}}$  (Y-axis). The data points are colour-coded according to the mergers' respective inspiral time until merger,  $\tau_{\text{insp}}$ , since their decoupling from the parent cluster (colour bar). For convenient visibility,  $\tau_{\text{insp}}$  values below  $\lesssim 1$  year share the same colour. The meaning of the different symbols is the same as in Fig. 4. **Right panel:** distribution (probability density function) of  $t_{\text{mrg}}$  shown for the in-cluster and ejected mergers separately (filled histograms), as well as for the combined merger population (empty histogram). The combined distribution is normalised to be integrated up to unity. The integrals of the in-cluster- and ejected-merger distributions are scaled according to the respective sub-population's count relative to the total merger count (so that the distributions add up to the normalised combined distribution).

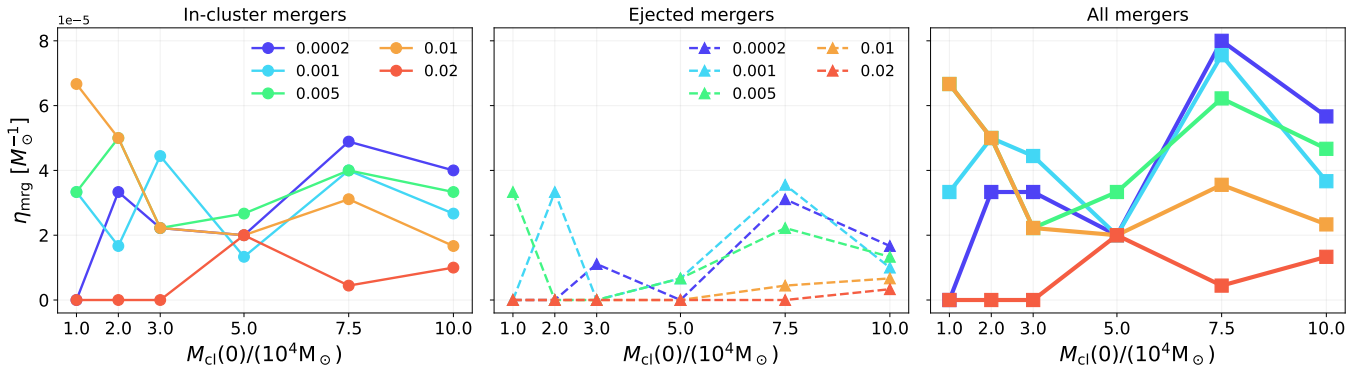


FIG. 6. Efficiency per unit initial cluster mass (Y-axis),  $\eta_{\text{mrg}}$ , of in-cluster (left panel), ejected (middle), and all (right) compact binary mergers as a function of cluster initial mass,  $M_{\text{cl}}(0)$  (X-axis), and metallicity,  $Z$  (legend), as obtained from the computed star cluster model grid in this work.

$\tau_{\text{insp}}$  for ejected mergers are calculated from the binaries' orbit-averaged GW decay starting from the state at the time of the ejection from the cluster. The  $t_{\text{mrg}}$  values are obtained by adding  $\tau_{\text{insp}}$  to the decoupling or the ejection time.

Fig. 5 (left panel) expectedly shows an overall anti-correlation between the model events'  $m_{\text{tot}}$  and  $t_{\text{mrg}}$ . Due to shorter mass segregation time [19], more massive BHs inside a cluster are dynamically processed earlier [94, 97]. Furthermore, more massive BBHs would generally have a shorter  $\tau_{\text{insp}}$  [90]. These, combined, give rise to this trend. For all in-cluster mergers,  $\tau_{\text{insp}} < 1$  Myr (colour coding), which is less than the typical gravitationally focused binary-single close interaction timescale [66] of  $\sim 1$  Myr among BHs in such clusters. Only for such small  $\tau_{\text{insp}}$  can an in-cluster binary successfully undergo GW inspiral and coalescence, before the inspiral gets inter-

rupted by an intruder. See Ref. [32] for further details and discussions (c.f. their Fig. 9).

In contrast, the ejected mergers can have large  $\tau_{\text{insp}}$  as they have up to the Hubble time (minus the ejection time) to coalesce. Fig. 5 (right panel) demonstrates the contrasting  $t_{\text{mrg}}$  distributions of the in-cluster and ejected mergers as obtained from the present models. While the in-cluster mergers take place mainly within  $t_{\text{mrg}} \lesssim 2$  Gyr (although their  $t_{\text{mrg}}$  distribution's tail is extended up to  $\approx 8$  Gyr), the ejected mergers have a much flatter  $t_{\text{mrg}}$  distribution extending up to the Hubble time.

Fig. 6 plots the GW merger efficiency per unit initial cluster mass,  $\eta_{\text{mrg}}$ , of the model clusters as a function of  $M_{\text{cl}}(0)$ , at the different metallicities. In this study,  $\eta_{\text{mrg}}$  of a population of clusters with total initial mass

$M_{\text{cl,tot}}(0)$  is defined as

$$\eta_{\text{mrg}} \equiv \frac{N_{\text{mrg,tot}}}{M_{\text{cl,tot}}(0)}, \quad (1)$$

where  $N_{\text{mrg,tot}}$  is the total number of GR mergers produced by that cluster population. In Fig. 6, the efficiency of in-cluster, ejected, and all mergers are shown separately (left, middle, and right panels, respectively). All the  $\eta_{\text{mrg}}$ s are marginalised with respect to the clusters'  $r_{\text{h}}(0)$ .

As seen in Fig. 6,  $\eta_{\text{mrg}}$  generally increases with decreasing  $Z$  at all  $M_{\text{cl}}(0)$  and for both in-cluster and escaped mergers. This is expected since at lower  $Z$  cluster-retained BHs are more massive and numerous, resulting in a denser and longer lasting BH core (Sec. III A; Fig. 2). Interestingly,  $\eta_{\text{mrg}}$  does not show a clear monotonic trend with  $M_{\text{cl}}(0)$ . Both in-cluster and ejected mergers exhibit a minimum at  $M_{\text{cl}}(0) = 3 \times 10^4 M_{\odot}$  or  $5 \times 10^4 M_{\odot}$  at all  $Z$  except at the highest  $Z = 0.02$ ; at  $Z = 0.02$ ,  $\eta_{\text{mrg}}$  maximises at  $M_{\text{cl}}(0) = 5 \times 10^4 M_{\odot}$ . Apart from the highest  $Z$  (that causes the lowest BH retention),  $\eta_{\text{mrg}}$  tends to maximise at  $M_{\text{cl}}(0) = 7.5 \times 10^5 M_{\odot}$  considering all mergers (Fig. 6, right panel). At the lowest  $M_{\text{cl}}(0) = 1.0 \times 10^4 M_{\odot}$ ,  $\eta_{\text{mrg}}$  attains comparable values at intermediate  $Z$ s but decreases at the lowest  $Z$ s. While the  $\eta_{\text{mrg}}$  values may have been affected by the limited number of events from the model grid, qualitatively similar trend with  $M_{\text{cl}}(0)$  is exhibited at most metallicities for both in-cluster and ejected mergers. This trend can be interpreted as the increasing competition, with increasing cluster mass, between the formation of a larger number of BBHs (at a given metallicity) and the cluster's increasing ability to interrupt or ionise them via close dynamical interactions. Notably, other studies such as Ref. [40] have also found non-monotonic behaviour of  $\eta_{\text{mrg}}$  with  $M_{\text{cl}}(0)$ .

Note that the total number of mergers from a cluster, overall, increases with the cluster's mass; see Table. III and Fig. 14. However, it is the merger efficiency that is directly relevant for estimating the merger rate [40, 94]. In basic terms, the merger rate is

$$R \propto \epsilon_{\text{CFE}} \psi_{\text{SFR}} \int_{M_{\text{cl}}} \eta_{\text{mrg}}(M_{\text{cl}}) \phi_{\text{CLMF}}(M_{\text{cl}}) dM_{\text{cl}}, \quad (2)$$

where  $\psi_{\text{SFR}}$  is the mass formation rate of stars (typically in  $M_{\odot} \text{ yr}^{-1} \text{ Mpc}^{-3}$ ),  $\epsilon_{\text{CFE}}$  is the cluster formation efficiency (hereafter CFE) that determines the fraction of star formation in the form of bound star clusters, and  $\phi_{\text{CLMF}}(M_{\text{cl}})$  is the distribution density function of the clusters' birth masses (typically taken as  $\propto M_{\text{cl}}^{-2}$ ). The calculation of GR merger rate from the present models is detailed in Appendix B.

#### IV. COMPARISONS WITH GWTC

Fig. 7 plots the model GW mergers' masses and compares them with the latest GWTC, *i.e.*, the catalogue

containing all GW events up to LVK's O4a (Sec. I). The plotted observed events (filled squares) are distinguished across false alarm rate (hereafter FAR) =  $1 \text{ yr}^{-1}$ . In the four panels, the model events (filled circles) are colour-coded according to their delay time, primary- and secondary-member dimensionless spin,  $a_1$  and  $a_2$  (Sec. II B, Appendix C), and parent-cluster metallicity. It is seen that the model mergers collectively agree well with the general trend of the observed events, considering the latter's 90% credibility intervals (hereafter CI; error bars). Apart from the general trend, the model events also well reproduce several outlier LVK events, especially those having a companion close to or within the LMG. This is a consequence of adopting the delayed remnant mass model (Sec. II B). Several of the (relatively) outlier BBH merger events are also reproduced by the model mergers. However, these model events do not reach the component masses of GW231123 – the to-date most massive observed BBH merger [98], although the most massive model merger's secondary mass is within the 90% CI of GW231123's secondary. Note that to avoid overcrowding, the model mergers in Fig. 7 are not distinguished as in-cluster/ejected or primordially/dynamically paired. However, the panels can be directly mapped onto Fig. 4 (left panel), which provides such information (Sec. III B).

The computed mergers have delay times of  $t_{\text{mrg}} \gtrsim 100$  Myr (see Sec. III B for a detailed discussion on  $t_{\text{mrg}}$ ) and they are produced predominantly by moderate- and low-metallicity clusters ( $Z \leq 0.01$ ). The latter is evident also from Table III. As for BH spins (Fig. 7, lower panels), the PSN-gap model BBH mergers can have highly spinning or low-spin components. The spin of BBH mergers with components in the PSN gap is of high interest owing to GW231123 and other massive GW events [18, 95, 98–101]. The present model PSN-gap mergers possess a wide range of spin morphology. They comprise systems with both components having high spin (like GW231123), a high-spin and a low-spin component, or both components having low spin. In the current set of model events, all PSN-gap mergers are dynamically paired and the majority of them are in-cluster.

Among the model BBH mergers that have a component within or near the LMG, highly asymmetric events ( $q \lesssim 0.5$ ) are found to be relatively common, with the primary having a high spin. Qualitatively, such events resemble the observed events GW241011 and GW241110 [102]<sup>4</sup>. In the present model event set, all (near) LMG mergers are primordially paired and ejected (see Sec. III B). Note that, at present, NBODY7 can runtime assign astrophysical-model-based spins only to a fraction of the BHs that are formed inside the cluster, namely, to those BHs that preserve their low natal spin of  $\lesssim 0.15$  or

<sup>4</sup> In this study, the events GW241011 and GW241110 are not plotted in Figs. 7 and 8 as they have not yet been included in the cumulative GWTC (as of January 2026). However, they are included in the full list of  $> 300$  events (all events, all versions).

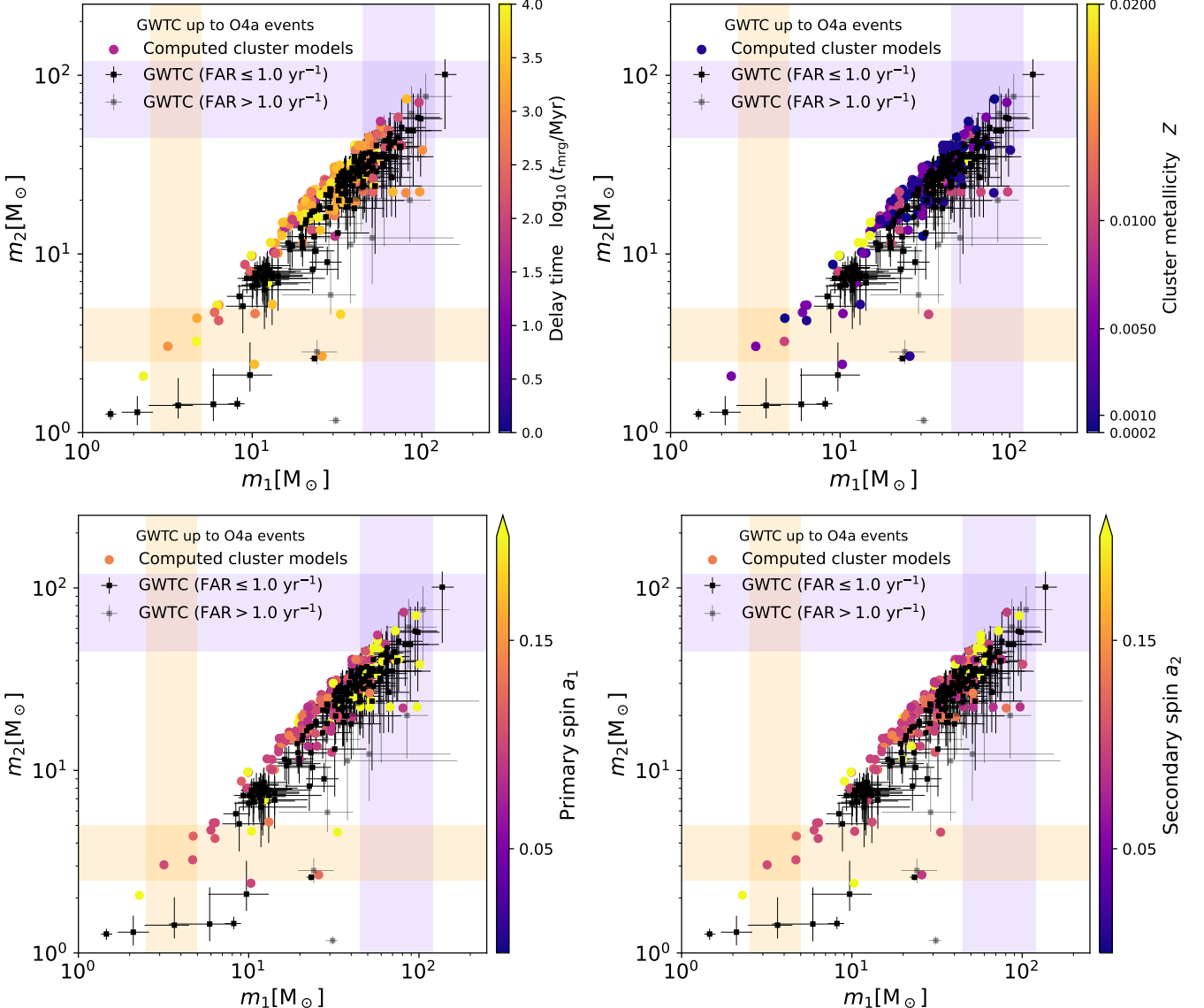


FIG. 7. Primary mass-secondary mass ( $m_1 - m_2$ ; see Fig. 4) plot of the GW coalescences produced by all the 90 evolutionary model clusters in this work (filled circles). The model-merger data points are colour-coded according to the mergers' delay time,  $t_{\text{mrg}}$  (upper left panel), parent-cluster metallicity,  $Z$  (upper right), primary-member dimensionless spin (or Kerr parameter),  $a_1$  (lower left), and secondary-member dimensionless spin,  $a_2$  (lower right). On each panel, the canonical NS-BH and PSN mass gaps (see Fig. 4) are indicated by filled patches. The spin-based colour coding is set such that a BH member with spin  $\lesssim 0.15$ , *i.e.*, preserving its natal spin, is represented by orange or a lower-valued colour. The remaining saturated-coloured members are candidates of possessing high spins. On each panel, events from the up-to-date, publicly available GWTC (the cumulative version) are overlaid for comparison (median values and the corresponding 90% CIs as filled squares and error bars, respectively). Among the GWTC events, only the astrophysical candidates, *i.e.*, those with  $p_{\text{astro}} > 0.5$  [2], are plotted that are furthermore distinguished across  $\text{FAR} = 1 \text{ yr}^{-1}$  (legend). No colour coding is applied to the GWTC data points. See text for further details.

that are outcomes of in-cluster BBH mergers (Sec. II B). However, spins of the high-spin BH candidates that are outcomes of close, internally interacting stellar binaries or that have undergone mass accretion have to be reassigned post-run. This procedure is detailed in Appendix C.

Fig. 8 (upper panels) plots the model BBH(-only)

mergers'  $m_{\text{tot}}$  and effective spin parameter,  $\chi_{\text{eff}}$  (X-axes), versus  $q$  (Y-axes) and compares them with the current GWTC. Here, the model data points corresponding to primordially paired mergers are indicated by a thick edge. The model data are colour-coded according to their respective parent clusters'  $M_{\text{cl}}(0)$ . It is seen that these mergers well encompass the wide  $q$ -range of the GWTC

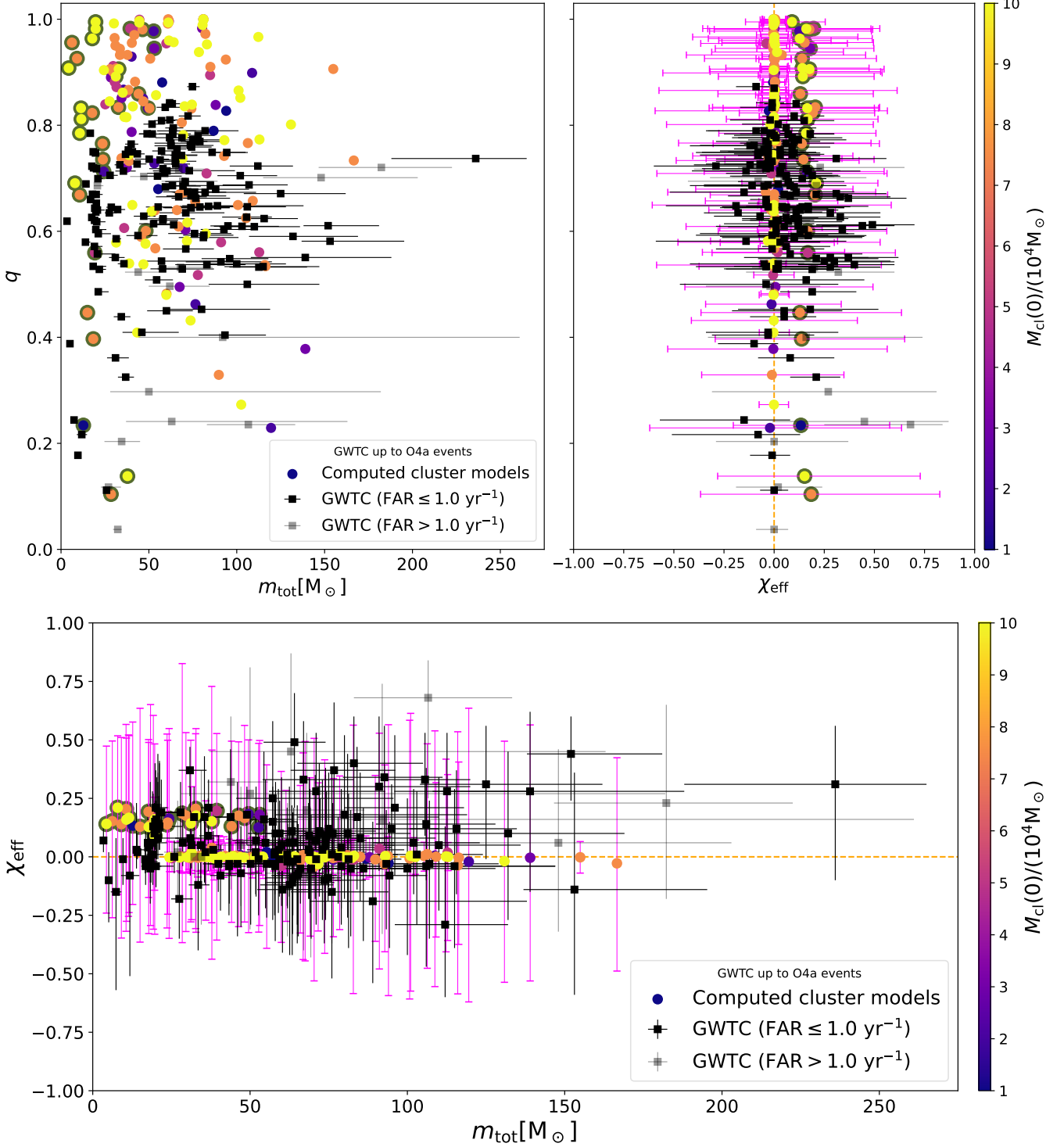


FIG. 8. **Filled circles:** The upper panels show total mass,  $m_{\text{tot}}$  (upper left), and effective spin parameter,  $\chi_{\text{eff}}$  (upper right), versus mass ratio,  $q$ , of the GW coalescences produced by all the computed model clusters in this work. The lower panel plots these mergers'  $m_{\text{tot}}$  versus  $\chi_{\text{eff}}$ . In all panels, the symbols are colour-coded with the initial mass,  $M_{\text{cl}}(0)$ , of the mergers' respective parent star cluster and the primordially paired mergers are marked with an additional thick-lined edge around their symbols. In the upper right and lower panels, each symbol and the associated magenta bar represent, respectively, the mean and the range (90% CI) of  $\chi_{\text{eff}}$  values for the possible range of spin-orbit orientation of the corresponding merger, after incorporating dynamical tilt (see Appendix C). **Filled squares with error bars:** On each panel, events from the current GWTC (cumulative version) are overlaid for comparison. The symbols and their error bars are plotted in the same way as in Fig. 7. The current publicly available catalogue does not explicitly contain the observed GW events' mass ratio values and their uncertainties. Therefore, in the upper panels, the GWTC events' median secondary mass to median primary mass ratio and no error bars are plotted along the vertical axis. See text for further details.

events. Asymmetric ( $q \lesssim 0.5$ ), dynamically paired mergers are often ( $\approx 50\%$  of them) produced by lower-mass clusters ( $M_{\text{cl}}(0) \leq 5 \times 10^4 M_{\odot}$ ). This is expected, since due to such clusters' relatively short relaxation and mass-segregation times [66], the mass segregation of the BHs in them is more rapid and complete, allowing for dynamical interactions over a wider BH mass range. See Sec. III B for more discussions on mass ratios of these model mergers.

The observable, effective spin parameter [103], is a measure of the spin-orbit alignment of the merging binary and is defined as

$$\chi_{\text{eff}} = \frac{(m_1 \vec{a}_1 + m_2 \vec{a}_2) \cdot \hat{L}}{m_1 + m_2} = \frac{(m_1 a_1 \hat{a}_1 \cdot \hat{L} + m_2 a_2 \hat{a}_2 \cdot \hat{L})}{m_1 + m_2} \quad (3)$$

or

$$\chi_{\text{eff}} = \frac{m_1 a_1 \cos \theta_1 + m_2 a_2 \cos \theta_2}{m_1 + m_2} = \frac{a_1 \cos \theta_1 + q a_2 \cos \theta_2}{1 + q}. \quad (4)$$

Here, the merging masses  $m_1, m_2$ , have, respectively, dimensionless spin vectors  $\vec{a}_1 = \hat{a}_1 a_1$ ,  $\vec{a}_2 = \hat{a}_2 a_2$ . They make angles  $\theta_1, \theta_2$ , respectively, with the direction of the orbital angular momentum,  $\vec{L}$ , defined by the unit vector  $\hat{L} \equiv \vec{L}/L$ <sup>5</sup>. During a GR inspiral,  $\chi_{\text{eff}}$  remains nearly invariant [104, 105]. Therefore, to a good approximation, one can apply  $\theta_1, \theta_2$  at the formation of the in-spiralling double compact binary to infer the LVK-measured  $\chi_{\text{eff}}$  at a later time, during the final GW inspiral.

In Fig. 8 (upper right panel), the model  $\chi_{\text{eff}}$  values are plotted by taking into account the possible range of spin-orbit inclination for both primordially paired and dynamically paired mergers. For the primordially paired events, the BH spins and the spin-orbit tilts are adopted from a reference model evolutionary massive binary population that incorporates formation of BHs with elevated spin from tidally spun-up Wolf-Rayet (hereafter WR) stars. They are furthermore subjected to additional spin-orbit tilts mimicking experiencing dynamical scatterings inside their parent cluster. For the dynamically paired events, an isotropic spin-orbit tilt distribution is always assumed for both components independently, after reassigning the spins of the high-spin BH candidates:  $(\cos \theta_1, \cos \theta_2) \in \mathcal{U}(-1, 1)$ , where  $\mathcal{U}(-1, 1)$  is the uniform distribution over  $[-1, 1]$ . The above procedures are detailed in Appendix C. In Fig. 8, the random choices of the tilt, azimuth, and spin (when applicable) values are repeated for 200 times for each model event to determine its sample  $\chi_{\text{eff}}$ s. The corresponding mean and range (90% CI) of a model event's  $\chi_{\text{eff}}$  are plotted as a filled circle and its error bar, respectively.

Owing to the preferential spin-orbit alignment even after incorporating dynamical tilt [106], the model primordially paired mergers are generally biased towards

$\chi_{\text{eff}} > 0$ . Considering the 90% CIs, the computed mergers'  $\chi_{\text{eff}}$  generally well encompass all the observed mergers. However, the model events seemingly do not exhibit any  $\chi_{\text{eff}} - q$  correlation (Fig. 8; upper right panel). Due to the substantial uncertainty in  $\chi_{\text{eff}}$  measurements, no significant  $\chi_{\text{eff}} - q$  dependence could be inferred from the to-date-observed GW events [17].

Fig. 8 (lower panel) exhibits a 'spin gap' along  $m_{\text{tot}}$  for the model events. For  $m_{\text{tot}} \lesssim 25 M_{\odot}$ , all mergers have positively biased  $\chi_{\text{eff}}$ , for  $25 M_{\odot} \lesssim m_{\text{tot}} \lesssim 60 M_{\odot}$ , there is a mixture of  $\chi_{\text{eff}}$ -positive-biased and  $\chi_{\text{eff}}$ -symmetric mergers, and for  $m_{\text{tot}} \gtrsim 60 M_{\odot}$ , all mergers are  $\chi_{\text{eff}}$ -symmetric. This is a consequence of switching from purely primordially paired to purely dynamically paired mergers with increasing merger mass (Fig. 4, Sec. III B). Among these patterns in the model event set, only that over the intermediate  $m_{\text{tot}}$  range generally agrees with GWTC. For the low  $m_{\text{tot}}$  range, the GWTC events'  $\chi_{\text{eff}}$  are systematically shifted from those of the model events, having smaller or negative values. For the high  $m_{\text{tot}}$  range, the GWTC events are generally positively biased compared to the model events. These discrepancies may suggest additional formation channels of the observed GW events, producing a diverse range of spin-orbit-alignment properties (see Sec. I and references therein).

### A. Comparisons with GW event population properties

To estimate the rate and properties of GW mergers in the Universe with redshift,  $z$ , due to the YMC/OC channel, a Model Universe is constructed out of the cluster model grid and its GW mergers. The Model Universe takes into account observation-based cluster birth mass function, observation-based cosmic star formation rate (hereafter SFR) and metallicity evolutions from  $z = 10$  up to  $z = 0$ , and the standard background cosmological model, as detailed in Appendix B. In this section, only the results are discussed.

In Fig. 9, the black-filled squares with blue bars show the Model Universe differential intrinsic merger rate density distribution with respect to primary mass (left panel) and mass ratio (right panel), at a fiducial redshift of  $z = 0.2$ . At each  $m_1$  or  $q$  bin, the bar spans between the standard and the pessimistic rate corresponding to that bin (Appendix B), and the filled square lies halfway between the two rates. For comparison, the corresponding LVK-obtained differential merger rate densities at the same redshift are co-plotted in the panels' background: here, the B – Spline and Broken Power Law + 2 peaks models from GWTC-4 and the Power Law + Peak model from GWTC-3 are shown. These background plots are the intact contents of Figs. 3 and 5 of Ref. [17].

It is seen that the model  $d\mathcal{R}/dm_1$ , overall, accommodates and follows the shape of the continuum structure of LVK's observed-event-based rate density distributions beyond  $m_1 \gtrsim 15 M_{\odot}$ . As in the LVK-inferred

<sup>5</sup> In this paper, a vector  $\vec{A}$  has magnitude  $A$  and the unit vector in its direction is denoted by  $\hat{A}$ .

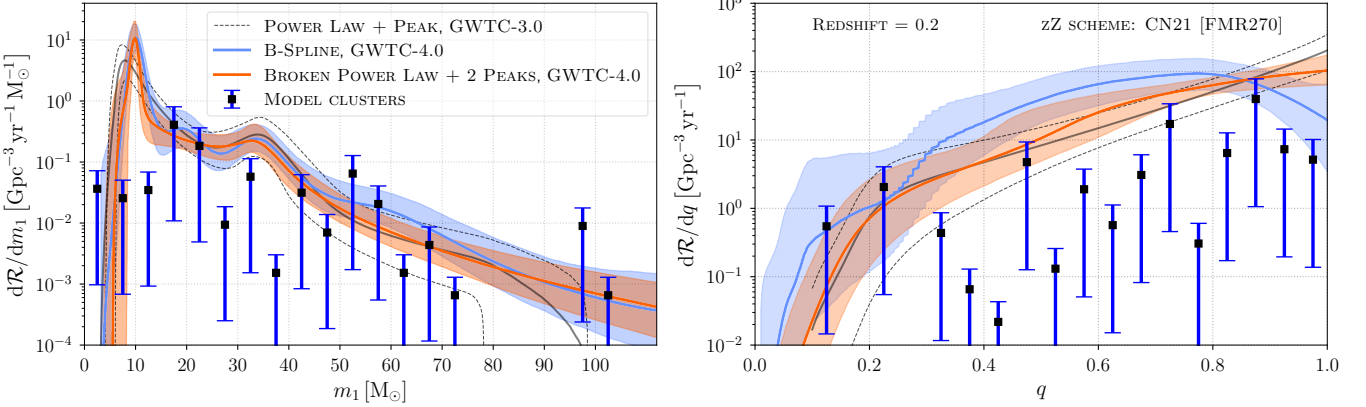


FIG. 9. **Black-filled squares with blue bars:** differential intrinsic merger rate density distribution at a fiducial redshift of  $z = 0.2$ , as derived from the model-merger population synthesis in this work (see Appendix B). At each bin, the bar spans between the standard and the pessimistic rate corresponding to that bin, and the filled square lies halfway between the rates. The left (right) panel plots the differential merger rate density with respect to the merger primary mass (mass ratio),  $d\mathcal{R}/dm_1$  ( $d\mathcal{R}/dq$ ). The model-cluster rate estimates presented here correspond to the CN21 redshift-metallicity ( $zZ$ ) scheme (Appendix B; Fig. 15). **Background overlays:** corresponding differential intrinsic merger rate density distributions at the same fiducial redshift, as inferred by LVK based on the GWTC-3 and GWTC-4 events, for different compact-remnant mass models (legend). The solid lines and the shaded areas correspond to the median and the 90% CI of the distributions, respectively. The corresponding LVK limits from GWTC-3 are also shown (thin, dashed, black lines). The data and the style of the overlays are adopted from the publicly accessible resources corresponding to Ref. [17] (see their Figs. 3 and 5) without applying any rescaling or normalisation to the rate values.

$m_1$ -distribution, the model distribution exhibits a peak at  $m_1 \approx 30M_\odot$ <sup>6</sup>. However, the Model Universe fails to produce a sharp, global peak at  $m_1 \approx 10M_\odot$ , unlike the observed distribution. Instead, the model rate density drops for  $m_1 \lesssim 15M_\odot$ . Such a drop in merger rate for low-mass mergers has been inferred also in other recent studies, *e.g.*, Ref. [42]. The computed models tend to overestimate the merger rate for  $m_1 \gtrsim 90M_\odot$ .

The model  $d\mathcal{R}/dq$  reasonably accommodates and follows the shape of the LVK's rate density distribution over the entire range of  $q$ . In particular, the model rate density distribution supports a maximum at  $q \approx 0.8$  as for the observed B-Spline distribution. Note that the model rates presented in Fig. 9 correspond to the CN21 redshift-metallicity ( $zZ$ ) dependence – see Appendix B for the details. Fig. 16 (Appendix D) similarly plots the model rate distributions for the other two  $zZ$  schemes considered in this study, namely, CN19 and MF17 (Appendix B). The above features of the model merger rate distributions generally remain valid also for these alternative  $zZ$  relations. The standard values of the integrated model intrinsic merger rate density at  $z = 0.2$  for the cases of CN19, CN21, and MF17  $zZ$  dependence are, respectively,  $9.9 \text{ yr}^{-1} \text{Gpc}^{-3}$ ,  $8.8 \text{ yr}^{-1} \text{Gpc}^{-3}$ , and  $7.3 \text{ yr}^{-1} \text{Gpc}^{-3}$ . This means that GW mergers from the present model clusters account for up to  $\approx 1/3$ rd of the LVK-inferred merger rate density [17].

The abrupt decay of the model  $d\mathcal{R}/dm_1$  for  $m_1 \lesssim 15M_\odot$  is due to the adoption of the delayed remnant mass model (Sec. II B). Owing to a monotonic growth of the SN fallback fraction in the delayed model beginning from the lowest mass BHs [54] and the consequent high natal kick for low-mass BHs, the retention of remnants of  $\lesssim 10M_\odot$  is unlikely in the present model clusters at all metallicities [49]. Therefore, dynamical pairing hardly contributes to GW mergers for  $m_1 \lesssim 10M_\odot$ , wherein mainly (escaped) primordially paired mergers alone contribute (c.f. Fig. 4)<sup>7</sup>. The  $30M_\odot$ -peak in the model rate distribution is likely caused by the mass distribution of cluster-retained BHs that possesses such a peak for the delayed remnant model, especially at low metallicities, combined with the more efficient mass segregation and dynamical pairing of such BHs compared to the lower-mass retained BHs – see Fig. 8 of Ref. [49].

Of course, the mass distribution of retained BHs is affected in the presence of a massive binary population due to various binary interactions or binary-mediated close dynamical interactions (*e.g.*, mass transfer between stellar components, mass accretion, star-star collisions). Fig. 17 (Appendix D) shows examples of cluster-retained BH mass distributions in the present models that exhibit

<sup>6</sup> This feature holds when the binning is altered.

<sup>7</sup> Although most ECS-NSs retain in the clusters, their mass segregation is quenched due to BH heating [67]. Even in the absence of BH heating, the NS sub-population in a cluster would not have formed a dynamically active central core [107], due to the NSs' much lower mass. Therefore, the NSs are typically unable to participate in dynamical pairing unlike the BHs.

prominent peaks at  $m_{\text{BH}} \approx 30M_{\odot}$  and  $40M_{\odot}$ , which are imprinted in the model  $d\mathcal{R}/dm_1$ . The distributions also demonstrate the sharp drop for  $m_{\text{BH}} \lesssim 15M_{\odot}$  as discussed above. The maximum of the model  $d\mathcal{R}/dq$  at  $q \approx 0.8$  is an imprint of the prominence of BBH mergers around this mass ratio (see, *e.g.*, Fig. 4).

## B. Evolution with redshift

In the context of GW formation channels and GW detection by future-generation detectors [108], redshift evolution of various GW-merger parameters and the merger rate are of interest. Fig. 10 shows the redshift evolution of merger primary mass, secondary mass, mass ratio, and merger rate as obtained from the Model Universes with the different  $zZ$  relations (Appendix B). The mean  $m_1$ ,  $m_2$ , and  $q$  of the model mergers evolve significantly for  $z \lesssim 0.7$ , beyond which they evolve much more slowly with  $z$ . The 76% CI (equivalent of the full width at half maximum of a Normal distribution) of the distributions of these quantities at increasing  $z$  exhibit substantially higher variability for  $z \lesssim 2$  than for beyond this  $z$ . The full range of  $m_1$  ( $m_2$ ) runs from the least massive merging remnant's mass ( $\approx 2.4M_{\odot}$  NS; Fig. 4) up to  $\approx 100M_{\odot}$  ( $\approx 70M_{\odot}$ ) at all  $z$  for the MF17 and CN21  $zZ$  cases; for CN19, the upper mass limits decay beyond  $z \approx 5$ . In fact, for CN19, the mean  $m_1$  and  $m_2$  also decline and deviate from the rest of the  $zZ$  cases, for  $z \gtrsim 6$ .

These deviations can be explained by the fact that the CN19  $zZ$  dependence is substantially metal-poorer compared to the CN21 and MF17 counterparts over the entire  $0 \leq z \leq 10$  (Fig. 15). Since the primordially paired mergers from the current model clusters are formed predominantly at low metallicities with shorter delay times (Figs. 4, 5, 7), the CN19 Model Universe is richest in primordially paired mergers at all  $z$ , and, at high  $z$ , primordially paired mergers are dominant for CN19. This is demonstrated in Fig. 18 (Appendix D); see below for further discussions. Since the primordially paired mergers are generally less massive than the dynamically paired mergers (Fig. 4), their increased fraction at high redshifts causes the merger masses to decline therein, for the CN19 case.

As for the mass ratio evolution, all the considered  $zZ$  schemes produce similar redshift evolutions. The  $q$ -distribution widens for  $z \lesssim 5$  (age of the Universe  $\gtrsim 1$  Gyr) and the full  $q$ -range is achieved for  $z \lesssim 3$ . This is due to the fact that the most asymmetric model mergers have delay times  $> 1$  Gyr (Fig. 7). Note that in all panels in Fig. 10, equal-frequency bins are taken along the redshift axis so that the evolutions of the means and the CIs are not affected by bin-to-bin member number variation.

Fig. 10 (lower right panel) plots the evolution of the Model Universe's intrinsic GW merger rate density with redshift, for the three  $zZ$  cases. The LVK-obtained, observed GW event-based rate density evolutions are plot-

ted in the background. Here, LVK's power law-based inferences for GWTC-3 and GWTC-4 [17] are shown, since the power-law model, namely,  $\mathcal{R}(z) = \mathcal{R}(0)(1+z)^{\kappa}$ , is simpler and is not explicitly affected by the limited number of detected events from near the instruments' visibility horizon. Furthermore, the form of the adopted cosmic SFR evolution [109] (Appendix B) is also shown on the same panel. To aid comparison of the  $z$ -dependence, all  $\mathcal{R}(z)$  curves are normalised relative to their respective  $\mathcal{R}(0)$ . (For the GWTC-3 and GWTC-4 curves, the scaling is applied with respect to the respective mean GWTC rates at  $z = 0$ .)

It is seen that the redshift evolutions of the model merger rates, overall, follow the GWTC-4 merger rate evolution up to  $z \approx 2$ . The redshift evolutions for the MF17, CN19, and CN21 merger rate densities are generally similar to each other and they all achieve their global maxima at  $z \approx 2$ , as for the SFR evolution. However, the model rates increase with redshift faster than the SFR, consistently with the GWTC-4 rate.

Fig. 11 shows the redshift evolution of the  $\chi_{\text{eff}}$ -distribution of BBH mergers from the CN21 Model Universe. Here,  $\chi_{\text{eff}}$  values of the model mergers are obtained in the same way as described in Sec. IV and Appendix C, *i.e.*, by partially post-processing the BH spins, assigning spin-orbit tilts based on isolated binary evolution and isotropic orientation distribution, and incorporating added tilt angles due to close dynamical encounters. However, since in a Model Universe each event represents a single instance, only a single set of random draws is applied per model BBH merger. (The present Model Universes contain  $\sim 10^6$  events each.)

It is seen that, at  $z = 0$ , the model  $\chi_{\text{eff}}$  distribution is moderately asymmetric and positively biased, with a positive mean  $\chi_{\text{eff}}$ ,  $\mu_{\text{eff}}$  (blue solid lines in Fig. 11). However,  $\mu_{\text{eff}}$  quickly declines to  $\approx 0$  at  $z \approx 0.15$  and remains vanishing with a gradual increasing trend until  $z = 1.5$ . Over the long redshift range,  $\mu_{\text{eff}}$  continues to increase until  $z \approx 6$  and begins to decrease thereafter. In general,  $\mu_{\text{eff}} \geq 0$  and the  $\chi_{\text{eff}}$  distribution is asymmetric and positively biased at all  $z$ , for the model BBH mergers. However, at all  $z$ , the  $\chi_{\text{eff}}$  distribution extends significantly also towards  $\chi_{\text{eff}} < 0$ .

Interestingly, the above low-redshift behaviour of  $\mu_{\text{eff}}$ , as obtained from the computed models, is consistent with LVK's GWTC-4-based inferences of the same. Especially, the small but positive value of  $\mu_{\text{eff}}$  at  $z = 0$  and its vanishing at  $z \approx 0.15$  are supported by the corresponding GWTC-4 **Spline** inference; see Fig. 14 of Ref. [17]. The width of the model  $\chi_{\text{eff}}$  distribution continues to increase up to  $z \approx 0.75$  as for the GWTC-4 inferences, but after a constriction feature over  $0.15 \lesssim z \lesssim 0.3$ . The existence of such a constriction feature is marginally supported by LVK's **Spline** model for GWTC-4.

The above features in the model  $\chi_{\text{eff}}$  distribution arise from how the fraction of primordially paired mergers evolves with  $z$  for these model mergers, which is shown in Fig. 18. The source of the positively biased  $\chi_{\text{eff}}$ -

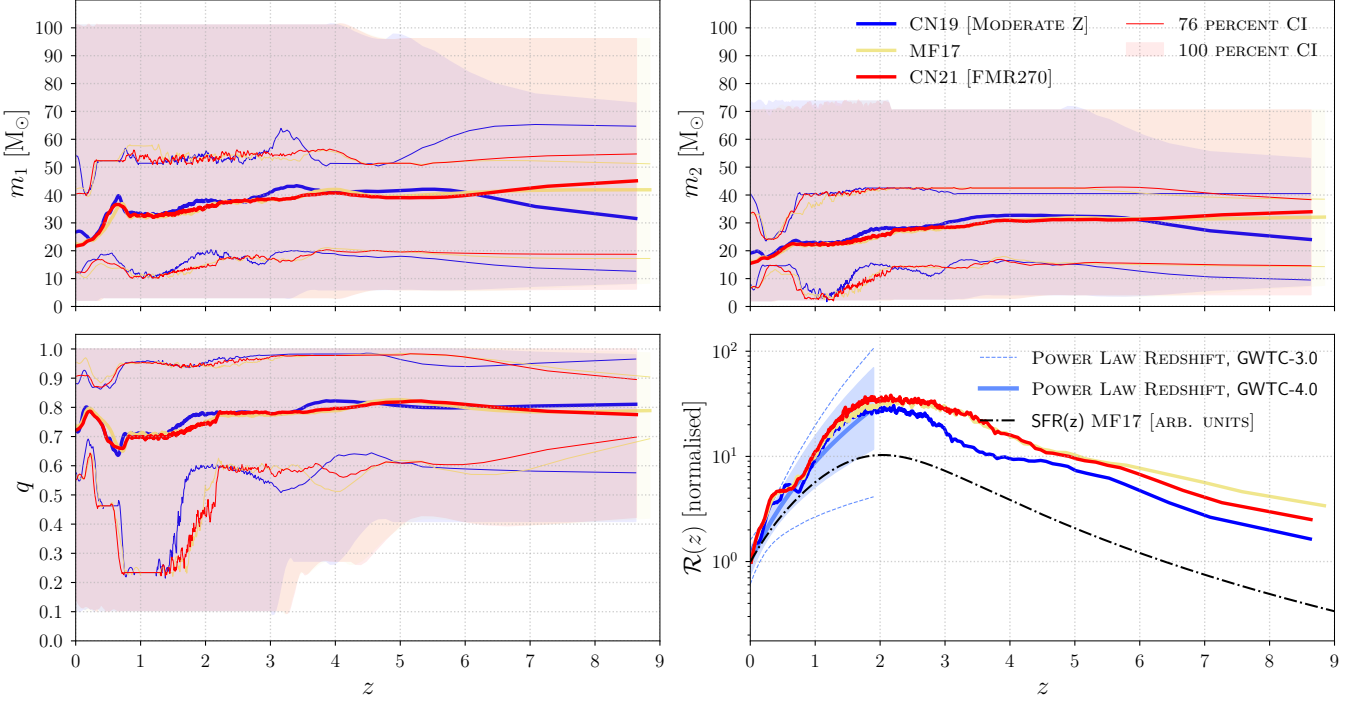


FIG. 10. Evolution of the distributions of various properties of model mergers with redshift,  $z$ . The upper left, upper right, lower left, and lower right panels show the redshift evolution of, respectively, merger primary mass, secondary mass, mass ratio, and the intrinsic merger rate density. The evolutions are shown for the different  $zZ$  schemes considered here, namely, MF17, CN19, and CN21 (Appendix B; Fig. 15), which are distinguished colour-wise as shown in the legend. In all but the lower right panels, for a particular  $zZ$  scheme, the thick line traces the mean value, the thin lines enclose the 76% CI, and the shaded area encloses the whole range of the distribution at increasing redshifts. **Lower right panel:** to facilitate comparison, each  $\mathcal{R}(z)$  curve is normalised with respect to its value at  $z = 0$ . The star formation rate density–redshift dependence of MF17 is also shown with an analogous normalisation (black dot-dashed curve). Overlaid in the background are the median (thick, solid, sky blue line) and 90% CI (blue-shaded region) of the intrinsic merger rate density evolution as obtained by LVK based on GWTC-4, which are, here, analogously scaled. The corresponding LVK limits from GWTC-3 are also shown (thin, dashed, sky blue lines). The data and the style of the overlays are adopted from the publicly accessible resources corresponding to Ref. [17] (see their Fig. 10).

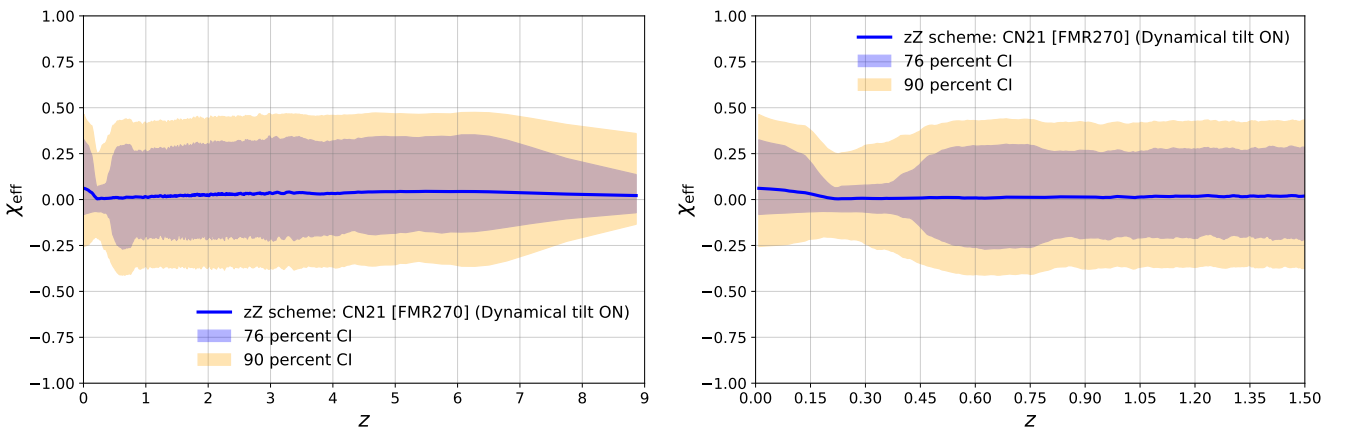


FIG. 11. Evolution of the effective spin parameter ( $\chi_{\text{eff}}$ ) distribution of model BBH mergers with redshift,  $z$ . **Left panel:** the thick, blue line traces the mean and the shaded regions enclose the 76% CI and 90% CI (legend) of the  $\chi_{\text{eff}}$  distribution at increasing redshifts. The evolution shown here corresponds to the CN21 redshift-metallicity ( $zZ$ ) dependence. For the case presented in this figure, dynamical tilt is incorporated in evaluating the model events'  $\chi_{\text{eff}}$ . **Right panel:** the same plot as in the left panel except that the X-axis is truncated at  $z = 1.5$ , for better visibility of the  $\chi_{\text{eff}}$  evolution at lower redshifts.

asymmetry is the primordially paired mergers that are modelled here with partially spin-orbit aligned tilt distributions for both of the merging members [68], based on model evolutionary massive binary populations (Appendix C). Although adding dynamical tilt widens the resultant tilt angle distributions and correspondingly increases the fraction of anti-aligned ( $\chi_{\text{eff}} < 0$ ) events, the overall tilt distributions remain preferentially aligned, resulting in a positively biased  $\chi_{\text{eff}}$  distribution [106]. Furthermore, the merging members of a primordially paired event potentially possess higher spin magnitudes due to tidal spin-up of the parent WR stars (Appendix C), leading to a wider (and positively biased; see above)  $\chi_{\text{eff}}$  distribution. On the other hand, the dynamically paired mergers are modelled with independent, isotropically oriented tilt distributions that necessarily cause a symmetric  $\chi_{\text{eff}}$  distribution with  $\mu_{\text{eff}} = 0$ . That way, the redshift-dependent mixing fraction of primordially paired mergers in Fig. 18 (CN21 panel) translates into the various features in Fig. 11.

In particular, the feature in Fig. 11 over  $0 \lesssim z \lesssim 0.15$  (see above) is due to the sharp rise of the primordially paired fraction for  $z \rightarrow 0$  over the same  $z$ -range in Fig. 18 (all panels). The latter feature is caused by the population of late-time ( $t_{\text{mrg}} \gtrsim 7$  Gyr) primordially paired mergers that the model grid has produced (Fig. 5). This is further demonstrated in Fig. 19 (Appendix D), where the delay time distributions of primordially paired and dynamically paired mergers are plotted separately. As seen, the primordially paired mergers are distributed within  $t_{\text{mrg}} \lesssim 4$  Gyr and beyond  $t_{\text{mrg}} \gtrsim 7$  Gyr, and the late subpopulation contributes to a similar extent as the dynamically paired mergers.

Fig. 20 (Appendix D) shows the redshift evolutions of the model-merger  $\chi_{\text{eff}}$  distribution for the cases of MF17 and CN19  $zZ$  dependence. All three  $zZ$  cases lead to qualitatively similar redshift evolutions. For CN19, the  $\chi_{\text{eff}}$ -asymmetry is distinctly higher than the other cases due to its higher primordially paired fraction across redshift (Fig. 18), as discussed above.

## V. COMPARISONS WITH GAIA BLACK HOLES AND NEUTRON STARS

Apart from GW observations, detached (*i.e.*, non-mass-transferring), compact-object–normal-star binaries, as discovered in the Galactic field by the Gaia mission, have the potential to provide clues regarding stellar remnant formation and the physics of the various channels through which such systems may have formed. The current model cluster grid has also produced detached BH-star and NS-star binaries that got ejected from the cluster and escaped to the galactic field. The formation mechanisms and the overall properties of these field BH-star binaries are similar to those found in earlier star cluster computations by the author. Hence, the discussion is not repeated here and the reader is encouraged to consult

Ref. [110] for the details. Fig. 12 shows the ejected black hole–main sequence star (hereafter BH-MS) binaries from the present model grid, distinguishing between dynamically paired and primordially paired systems. Consistently with the previous work (see also Refs. [111, 112]), the parameters of the dynamically paired field BH-MS binaries from the model clusters encompass those of the observed, detached BH-MS binary candidates Gaia-BH1 [113, 114] and Gaia-BH3 [115] in the MW field. However, the parameters of the primordially paired ones disagree with these observed binaries’ parameters. For Gaia-BH1, the disagreement is primarily due to its low component-star mass that the primordially paired BH-MS binaries hardly possess. For Gaia-BH3, the disagreement with the primordially paired systems is due to the binary’s low component-star mass, high BH mass, and long orbital period.

The total formation efficiency<sup>8</sup> of field BH-MS binaries with a low-mass ( $< 3M_{\odot}$ ) main sequence (hereafter MS) companion from the present grid is  $6.3 \times 10^{-6} M_{\odot}^{-1}$ . Restricting to only solar-mass-like ( $0.7M_{\odot} - 1.1M_{\odot}$ ) MS companions, the formation efficiency is  $7.0 \times 10^{-7} M_{\odot}^{-1}$ . The vast majority (96%) of the escaped BH-MS binaries containing a low-mass MS companion are dynamically paired (see Fig. 12). As discussed in Ref. [110], the rather low formation efficiency of escaped BH-star binaries is due to dynamically interacting BH-star systems inside the clusters favourably undergoing exchange interactions to become a BBH. Note that the above formation efficiencies are somewhat lower than the corresponding formation efficiencies reported in Ref. [31]. This is expected, since the tidally truncated, lower-mass model clusters in the above study generally dissolve at a faster rate, allowing a larger number of BH-star systems to escape in the field.

Fig. 13 plots the parameters of the ejected neutron star–main sequence star (hereafter NS-MS) binaries from the present model grid, distinguishing between dynamically paired and primordially paired systems. Overplotted in the panels are the Gaia-detected detached NS-MS binary candidates in the MW field that are reported in Ref. [116]. The dynamically paired field NS-MS binaries from the model clusters well encompass the Gaia NS binaries in terms of the ranges of NS mass, companion mass, and eccentricity. However, unlike the model NS-MS binaries, the observed systems have orbital periods  $< 10^3$  days. It is possible that wider NS-MS systems have remained undetected by Gaia until now. The primordially paired field NS-MS binaries also reasonably encompass the Gaia NS systems. However, there is a distinct subpopulation of primordially paired NS-MS systems with NS masses beyond the Gaia NS masses, of  $> 2M_{\odot}$ , and massive companion masses of  $> 10M_{\odot}$ . However, such massive NS-MS systems are not expected in the Gaia sample reported in Ref. [116], which authors

<sup>8</sup> Defined analogously to Eqn. 1.

TABLE II. Summary of the total formation efficiencies of escaped BH-MS and NS-MS binaries as obtained from the computed model cluster grid in this study.

Binary type	Low-mass companion ( $< 3M_{\odot}$ ) [ $M_{\odot}^{-1}$ ]	Solar-mass companion ( $0.7M_{\odot} - 1.1M_{\odot}$ ) [ $M_{\odot}^{-1}$ ]
BH-MS	$6.3 \times 10^{-6}$	$7.0 \times 10^{-7}$
NS-MS	$3.0 \times 10^{-6}$	$1.2 \times 10^{-6}$

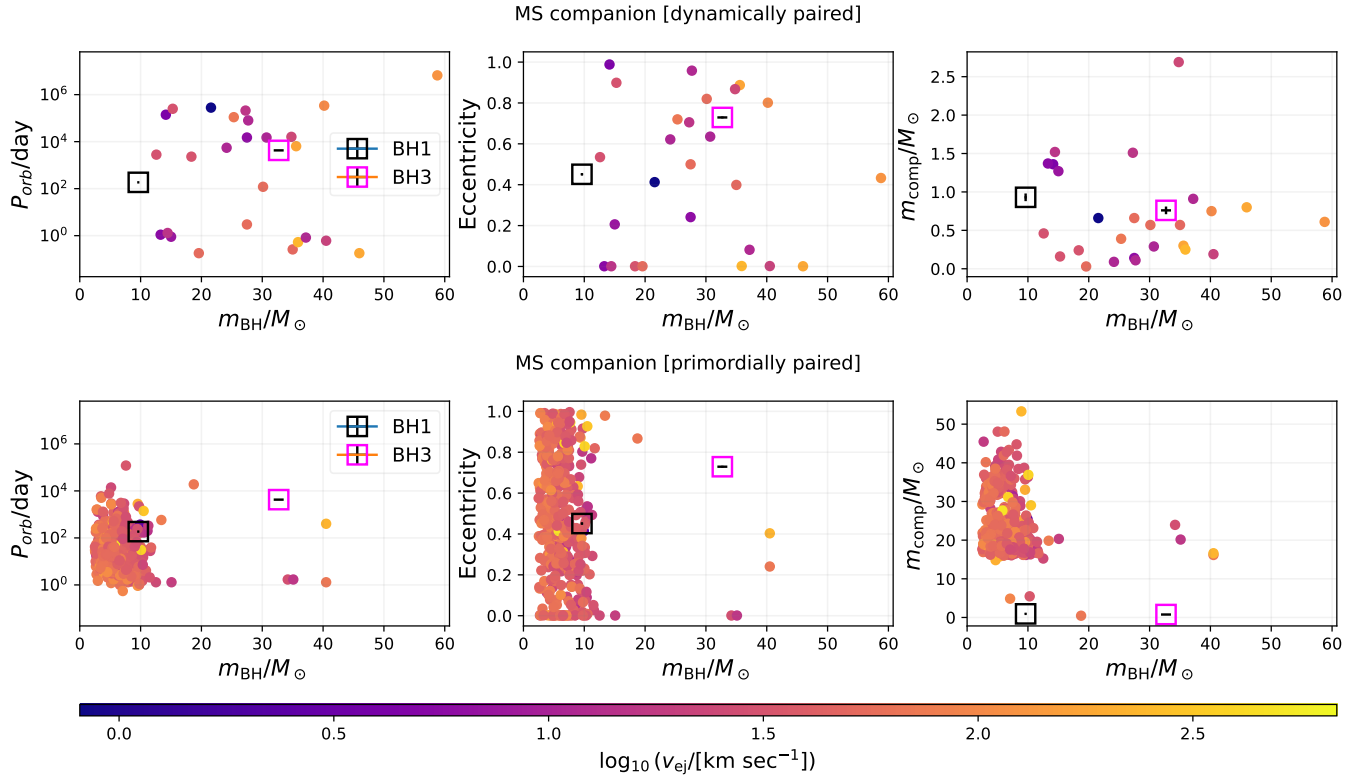


FIG. 12. Demographics of the BH-MS binaries that have escaped into the galactic field from the evolutionary model star clusters in this study. In each row, the filled circles in the panels plot the mass of the BH member ( $m_{\text{BH}}$ ; X-axes) against the orbital period ( $P_{\text{orb}}$ ; left panel), eccentricity (middle), and companion-star mass ( $m_{\text{comp}}$ ; right) of these model BH-MS binaries. The binaries are plotted separately depending on whether they are dynamically or primordially paired, as indicated in each row's title. The data points are colour-coded according to the velocity,  $v_{\text{ej}}$ , of the binary's ejection (colour bar). All plotted values correspond to the event of the binary's crossing of the instantaneous tidal lobe of its parent cluster. For comparison, the observed BH-MS binary candidates Gaia BH1 and Gaia BH3 are shown in each panel (empty squares). For these observed data points, the colour coding is not followed and their uncertainties are marginally visible due to the scale of the figure axes. (The size of the squares are chosen for legibility and does not represent measurement uncertainties.)

have restricted to only systems with low-mass MS companions. Systems with such massive companions are anyway unlikely to be detected owing to their short lifetimes and poor proper motion of the luminous member around the binary's barycenter.

Interestingly, the Gaia NS sample's mass distribution is statistically consistent with a narrow component at  $\approx 1.3M_{\odot}$  along with an extended component up to  $\approx 2M_{\odot}$  [117]. This is indeed supported by these model dynamically paired and primordially paired NS-MS systems with low-mass components (Fig. 13). For the dynamically paired systems, the  $\approx 1.3M_{\odot}$  NSs are ECS-NSs that retain in the clusters due to their small natal

kicks (Sec. II B). The total formation efficiency of field NS-MS binaries with a low-mass ( $< 3M_{\odot}$ ) MS companion from the present grid is  $3.0 \times 10^{-6} M_{\odot}^{-1}$ . Considering only solar-mass-like ( $0.7M_{\odot} - 1.1M_{\odot}$ ) MS companions, the formation efficiency is  $1.2 \times 10^{-6} M_{\odot}^{-1}$ . A moderate majority (61.5%) of the escaped NS-MS binaries containing a low-mass MS companion are dynamically paired (see Fig. 13). Table II summarises the above-mentioned model formation efficiencies of field BH-MS and NS-MS binaries.

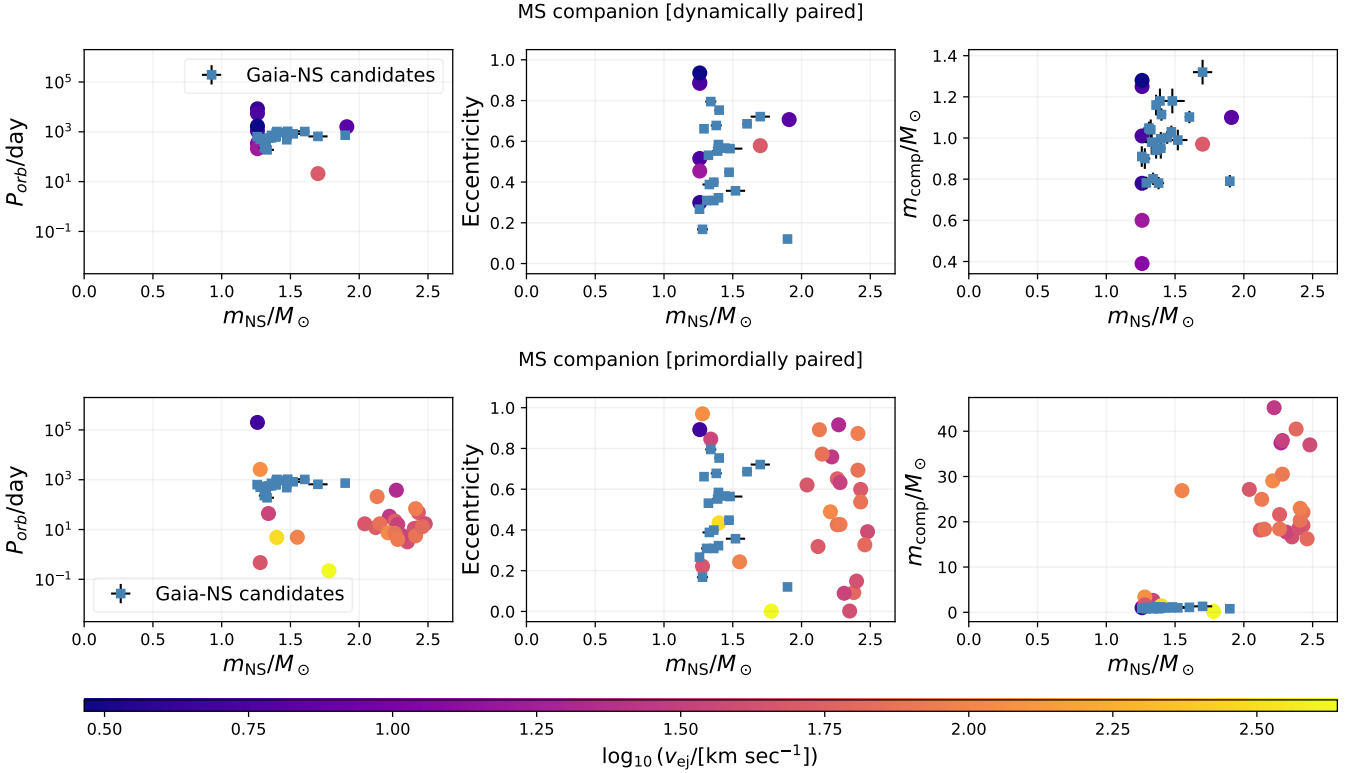


FIG. 13. Demographics of the NS-MS binaries that have escaped into the galactic field from the evolutionary model star clusters in this study. For the filled circles, descriptions analogous to Fig. 12 apply. For comparison, Gaia-observed NS-MS binary candidates are shown in each panel (filled squares). For these observed data points, the colour coding is not followed.

## VI. SUMMARY AND DISCUSSIONS

The properties of the to-date-observed GW-event candidates by the LVK and of their population suggest multiple role-playing formation channels for the merging compact binaries in the Universe, rather than a single dominant channel (Sec. I). This study surveys the role of young massive clusters evolving into intermediate mass ( $\sim 10^3 M_{\odot} - 10^4 M_{\odot}$ ), old open clusters, namely, the YMC/OC channel in forming GW mergers. To that end, a grid of 90 model star clusters of homogeneous properties, over the initial mass range  $10^4 M_{\odot} \leq M_{\text{cl}}(0) \leq 10^5 M_{\odot}$ , initial size range  $1 \text{ pc} \leq r_h(0) \leq 3 \text{ pc}$ , and metallicity range  $0.0002 \leq Z \leq 0.02$  are evolved for long term until most of the BHs are depleted from the clusters (Sec. II A, Fig. 1, Table III). The model-cluster set considered in this study, therefore, serves as a bridge between low-mass star clusters and massive GCs (Sec. I). The models incorporate an observationally motivated population of primordial binaries, the delayed stellar remnant mass model, black hole spins based on stellar evolution models, and in-cluster GR recoil kicks. They are evolved with a customised version of NBODY7, a star-by-star-resolution N-body integrator that incorporates stellar and binary evolution, stellar remnant formation, PN evolution of compact binaries, and collisions among stars

and stellar remnants (Sec. II B). The computed model clusters are generally consistent with the massive and compact star clusters of the Milky Way and Local Group galaxies across ages (Sec. III A, Fig. 3). The goal of this work is to assess to what extent the YMC/OC channel can explain the properties of the GW events observed to date, and whether it can simultaneously explain the compact star–normal star binaries discovered by the Gaia mission.

The main conclusions from this study are as follows:

- The GW mergers produced by the computed model cluster grid are primarily dynamically paired and take place inside the clusters (Sec. III B, Table I, Fig. 4). On the other hand, among the fewer escaped mergers, primordially paired systems are common. The vast majority of the model mergers are BBHs. While, overall, the mergers are biased towards having a symmetric mass ratio, asymmetric mergers are rather common: the dynamically (primordially) paired mergers extend down to a mass ratio of  $q \approx 0.2$  (0.1). With increasing primary mass, the model merger set switches from being predominantly primordially paired and escaped to being predominantly dynamically paired and in-cluster across  $m_1 \approx 10 M_{\odot}$ .

- The GW merger efficiency,  $\eta_{\text{mrg}}$ , of the model clusters exhibits a non-monotonic behaviour with  $M_{\text{cl}}(0)$ , for both in-cluster and ejected events (Sec. III B, Fig. 6). At all metallicities except  $Z = 0.02$ ,  $\eta_{\text{mrg}}$  reaches a maximum at  $M_{\text{cl}}(0) = 7.5 \times 10^5 M_{\odot}$ . The  $\eta_{\text{mrg}}$  for  $M_{\text{cl}}(0) \leq 3.0 \times 10^4 M_{\odot}$  is comparable to that for  $M_{\text{cl}}(0) \geq 7.5 \times 10^4 M_{\odot}$ , at most metallicities. The values of  $\eta_{\text{mrg}}$  are generally of order  $10^{-5}$ , which is consistent with the outcomes of N-body simulations by recent authors (see Ref. [31] for a discussion). Such  $M_{\text{cl}}(0)$  dependence of  $\eta_{\text{mrg}}$  suggests that the cluster mass range covered in this study is not exhaustive for GW-forming, sub-GC-mass star clusters that are gas-free and parsec scale, and the GW-formation threshold of such star clusters potentially lies at a lower mass. This means that the contributions of sub-GC-mass, parsec-scale, gas-free star clusters towards GW sources in the Universe as obtained from the current model set are potentially lower limits.
- The present model cluster grid produces GW mergers that agree with not only the mainstream events of the current GWTC but also GWTC's outlier low-mass (*e.g.*, highly asymmetric, involving a low-mass BH and a highly spinning primary BH like GW241011/GW241110) and high-mass (*e.g.*, double PSN-gap, highly spinning BH and misaligned like GW231123) events (Sec. IV, Figs. 7, 8). The most massive merger from the present model set is of  $m_{\text{tot}} \approx 166 M_{\odot}$ .
- The GW mergers from the current model grid well accommodate LVK's GWTC-4-based differential merger rate density beyond  $m_1 \gtrsim 15 M_{\odot}$  and exhibit notable features of LVK's mass distribution such as the peak at  $m_1 \approx 30 M_{\odot}$  (Sec. IV A, Appendix B, Fig. 9). The model mergers also well accommodate LVK's differential merger rate density w.r.t. mass ratio and reproduce its overall shape, including the broad peak around  $q \approx 0.8$  and merger rate density extending down to  $q \approx 0.1$ . However, the mergers fail to reproduce the sharp global peak of LVK's mass distribution at  $m_1 \approx 10 M_{\odot}$ , due to a dearth of events involving  $\approx 10 M_{\odot}$  BHs. This suggests that this feature of the GWTC population mass distribution is potentially associated with alternative GW-source formation channels such as isolated binary evolution, massive GCs, and nuclear clusters.
- The above features of the model merger rate density distributions hold for largely different cosmic redshift-metallicity ( $zZ$ ) dependence (Appendix B; Figs. 15, 16). Depending on the  $zZ$  relation, the total intrinsic GW merger rate density from the model cluster grid ranges over  $7.3 \text{ yr}^{-1} \text{Gpc}^{-3} - 9.9 \text{ yr}^{-1} \text{Gpc}^{-3}$  (standard, unscaled value) at a fiducial redshift of 0.2 (wherein LVK's GWTC-4-based differential and total merger rate densities are reported; Sec. IV A). Hence, YMC/OCs contribute  $\approx 25\% - 33\%$  of the total observed merger rate density, as obtained from these cluster models.
- The model total merger rate density increases with redshift moderately faster than the cosmic SFR evolution and consistently with the overall growth rate of GWTC-4 merger rate density, for  $z \lesssim 2$  (Sec. IV B, Fig. 10). The mass distribution of the model mergers evolves at low redshifts, over  $z \lesssim 0.7$ , wherein the mean merger primary and secondary masses increase with redshift. Beyond this redshift, the mass distributions evolve much more slowly. The model mergers' mass ratio distribution shows non-monotonic variability up to  $z \approx 2$ , beyond which it becomes approximately steady. The redshift evolutions are, overall, similar for the different  $zZ$  relations considered here.
- The effective spin parameter ( $\chi_{\text{eff}}$ ) distribution of the model BBH mergers is generally mildly asymmetric and positively biased at all redshifts, owing to the presence of primordially paired mergers (Sec. IV B, Fig. 11) that are partially spin-orbit aligned. Over redshift, the varied mixing fractions of primordially paired and dynamically paired mergers (Fig. 18) give rise to various features in the model-merger  $\chi_{\text{eff}}$  distribution. Some of these features are reminiscent of features present in LVK's GWTC-4-based  $\chi_{\text{eff}}$ -redshift dependence, *e.g.*, the positive asymmetry and notch near  $z \approx 0$  and the increasing width of the  $\chi_{\text{eff}}$  distribution up to  $z \approx 0.75$ . The model redshift evolution of  $\chi_{\text{eff}}$  distribution is qualitatively similar for the different  $zZ$  relations (Fig. 20).
- The model star cluster grid produces BH-MS and NS-MS binaries that escape into the galactic field. A fraction of the field model BH-MS and NS-MS systems is consistent with the parameters of the BH-MS and NS-MS candidates in the Galactic field as detected by the Gaia mission (Sec. V, Figs. 12, 13).

Notably, the model GW merger rate density obtained here is lower than that estimated for the YMC/OC channel in an earlier study by the author that applied a similar methodology [29]. This difference is possibly due to a combination of several aspects that were different in the earlier work, especially the use of an experimental, heterogeneous grid of model clusters that are biased towards higher cluster mass and BH retention, and the adoption of the rapid remnant mass model that causes higher BH retentions than the delayed counterpart [49]. Furthermore, the present rate estimates focus on a specific redshift, rather than the cosmic comoving volume within an assigned visibility boundary as was done in the earlier study.

A drawback of the present work is the adoption of (near-) spherical, virialised, gas-free initial star cluster models (Sec. II). Such initial conditions are in contrast with highly substructural, non-equilibrium, gas-rich conditions in star-forming regions [118, 119]. Effectively, the present, idealised initial condition associates itself with a certain cluster formation efficiency (CFE),  $\epsilon_{\text{CFE}}$  (Eqn. 2), *i.e.*, the fraction involved in assembling gas-free, near-spherical, (typically) parsec-scale, bound young star clusters that we observe in our and other galaxies, out of the total population of forming stars. The reader is directed to Ref. [31] and references therein for more detailed discussions on this regard, which is omitted here for brevity. Although the scaling procedure for obtaining GW merger rate densities, as described in Appendix B, does not explicitly assume a  $\epsilon_{\text{CFE}}$ , it implicitly assumes that  $\epsilon_{\text{CFE}}$  is invariant with redshift.

An important improvement to the current modelling is to implement the formation of tidally spun-up BHs and the assignment of binary-evolution-based tilts to primordially paired mergers during runtime. This would make the GW-merger treatment in the model clusters more consistent. For more complete merger rate estimates, it is important to incorporate star clusters over a wider mass range (*i.e.*, include GCs, nuclear star clusters, and low-mass clusters) and also field binaries. Such endeavours will be undertaken in the near future.

This study highlights the importance of intermediate-mass star clusters, which bridge low-mass clusters and associations to massive globular clusters, in forming GW mergers in the Universe. The work shows that they would have a role-playing contribution in shaping the GW-merger population's mass and spin distributions and the GW merger rate.

## DATA AVAILABILITY

The GW merger data and the data corresponding to the BH-star and NS-star binaries from the model clusters

will be made publicly available upon publication.

## ACKNOWLEDGMENTS

The author (SB) thanks Chris Belczynski (late), Aleksandra Olejak, Koushik Sen, Daniel Marin Pina, Iwona Kotko, Fabio Antonini, Mark Gieles, Norbert Langer for relevant discussions at various occasions. SB acknowledges funding for this work by the Deutsche Forschungsgemeinschaft (DFG; German Research Foundation) through the project “The dynamics of stellar-mass black holes in dense stellar systems and their role in gravitational wave generation” (project number 405620641; PI: S. Banerjee). SB has performed all of the  $N$ -body simulations reported in this work, analysed the data, prepared the illustrations, and written the manuscript. A part of the  $N$ -body simulations have been carried out on the `gpudyn`-series GPU computing servers containing NVIDIA Ampere A40 and NVIDIA RTX 2080 GPUs, located at the Argelander-Institut für Astronomie (AIfA), University of Bonn. The `gpudyn` servers have been sponsored by the above-mentioned DFG project, HISKP, and the University of Bonn. A part of the  $N$ -body simulations have been carried out on the Marvin HPC cluster (A40 GPU nodes) of the University of Bonn. SB acknowledges the access to the Marvin cluster of the University of Bonn. SB is thankful to the IT teams of the AIfA, HISKP, and the University of Bonn HPC center for their generous support. SB thanks the administrators of the AIfA for providing hospitality. SB acknowledges the use of artificial intelligence (AI) in this work for the following purposes: general proofreading (Apple Intelligence), machine-readable table compilation from publicly accessible resources for the observed data in Figures 3 and 13 (ChatGPT-5.2), bug fixing and optimisations in Python scripts (ChatGPT-5.2), fact-checking and literature search (Scholar AI). This work does not use any AI-generated content.

---

[1] R. Abbott, T. D. Abbott, F. Acernese, K. Ackley, C. Adams, N. Adhikari, R. X. Adhikari, V. B. Adya, and et al., *Physical Review X* **13**, 041039 (2023), arXiv:2111.03606 [gr-qc].

[2] The LIGO Scientific Collaboration, the Virgo Collaboration, the KAGRA Collaboration, A. G. Abac, I. Abouelfettouh, F. Acernese, K. Ackley, C. Adamcewicz, S. Adhikary, D. Adhikari, N. Adhikari, and et al., arXiv e-prints , arXiv:2508.18082 (2025), arXiv:2508.18082 [gr-qc].

[3] I. Mandel and F. S. Broekgaarden, *Living Reviews in Relativity* **25**, 1 (2022), arXiv:2107.14239 [astro-ph.HE].

[4] M. Spera, A. A. Trani, and M. Mencagli, *Galaxies* **10**, 76 (2022), arXiv:2206.15392 [astro-ph.HE].

[5] S. R. Kulkarni, P. Hut, and S. McMillan, *Nature* **364**, 421 (1993).

[6] H. M. Lee, *MNRAS* **272**, 605 (1995), arXiv:2412.14022 [astro-ph.SR].

[7] M. J. Benacquista and J. M. B. Downing, *Living Reviews in Relativity* **16**, 4 (2013), arXiv:1110.4423 [astro-ph.SR].

[8] K. Belczynski, V. Kalogera, and T. Bulik, *ApJ* **572**, 407 (2002), astro-ph/0111452.

[9] B. McKernan, K. E. S. Ford, J. Bellovary, N. W. C. Leigh, Z. Haiman, B. Kocsis, W. Lyra, M. M. Mac Low, B. Metzger, M. O'Dowd, S. Endlich, and D. J. Rosen, *ApJ* **866**, 66 (2018), arXiv:1702.07818 [astro-ph.HE].

[10] M. P. Vaccaro, M. Mapelli, C. Périgois, D. Barone, M. C. Artale, M. Dall'Amico, G. Iorio, and S. Torniamenti, *A&A* **685**, A51 (2024), arXiv:2311.18548 [astro-ph.HE].

[11] A. Vigna-Gómez, S. Toonen, E. Ramirez-Ruiz, N. W. C. Leigh, J. Riley, and C.-J. Haster, *ApJL* **907**, L19 (2021), arXiv:2010.13669 [astro-ph.HE].

[12] J. Stegmann, F. Antonini, and M. Moe, *MNRAS* **516**, 1406 (2022), arXiv:2112.10786 [astro-ph.SR].

[13] E. Michaely and H. B. Perets, *ApJL* **887**, L36 (2019), arXiv:1902.01864 [astro-ph.SR].

[14] C. Hamilton and R. R. Rafikov, *ApJL* **881**, L13 (2019), arXiv:1907.00994 [astro-ph.GA].

[15] J. Stegmann, A. Vigna-Gómez, A. Rantala, T. Wagg, L. Zwick, M. Renzo, L. A. C. van Son, S. E. de Mink, and S. D. M. White, *ApJL* **972**, L19 (2024), arXiv:2405.02912 [astro-ph.GA].

[16] M. Zevin, S. S. Bavera, C. P. L. Berry, V. Kalogera, T. Fragos, P. Marchant, C. L. Rodriguez, F. Antonini, D. E. Holz, and C. Pankow, *ApJ* **910**, 152 (2021), arXiv:2011.10057 [astro-ph.HE].

[17] The LIGO Scientific Collaboration, the Virgo Collaboration, the KAGRA Collaboration, A. G. Abac, I. Abouelfetouh, F. Acernese, K. Ackley, C. Adamciewicz, S. Adhikary, D. Adhikari, N. Adhikari, and et al., arXiv e-prints , arXiv:2508.18083 (2025), arXiv:2508.18083 [astro-ph.HE].

[18] S. Banagiri, E. Thrane, and P. D. Lasky, arXiv e-prints , arXiv:2509.15646 (2025), arXiv:2509.15646 [astro-ph.HE].

[19] S. Banerjee, H. Baumgardt, and P. Kroupa, *MNRAS* **402**, 371 (2010), arXiv:0910.3954 [astro-ph.SR].

[20] S. J. Aarseth, *MNRAS* **422**, 841 (2012), arXiv:1202.4688 [astro-ph.SR].

[21] S. Banerjee, *MNRAS* **467**, 524 (2017), arXiv:1611.09357 [astro-ph.HE].

[22] U. N. Di Carlo, N. Giacobbo, M. Mapelli, M. Pasquato, M. Spera, L. Wang, and F. Haardt, *MNRAS* **487**, 2947 (2019), arXiv:1901.00863 [astro-ph.HE].

[23] S. F. Portegies Zwart, S. L. W. McMillan, and M. Gieles, *ARA&A* **48**, 431 (2010), arXiv:1002.1961.

[24] M. R. Krumholz, C. F. McKee, and J. Bland - Hawthorn, *ARA&A* **57**, 227 (2019), arXiv:1812.01615 [astro-ph.GA].

[25] C. L. Rodriguez, K. Kremer, S. Chatterjee, G. Fragione, A. Loeb, F. A. Rasio, N. C. Weatherford, and C. S. Ye, *Research Notes of the American Astronomical Society* **5**, 19 (2021), arXiv:2101.07793 [astro-ph.HE].

[26] C. S. Ye, M. Fishbach, K. Kremer, and M. Reina-Campos, arXiv e-prints , arXiv:2507.07183 (2025), arXiv:2507.07183 [astro-ph.HE].

[27] F. Santoliquido, M. Mapelli, Y. Bouffanais, N. Giacobbo, U. N. Di Carlo, S. Rastello, M. C. Artale, and A. Ballone, *ApJ* **898**, 152 (2020), arXiv:2004.09533 [astro-ph.HE].

[28] J. Kumamoto, M. S. Fujii, and A. Tanikawa, *MNRAS* **495**, 4268 (2020), arXiv:2001.10690 [astro-ph.HE].

[29] S. Banerjee, *MNRAS* **503**, 3371 (2021), arXiv:2011.07000 [astro-ph.HE].

[30] G. Fragione and S. Banerjee, *ApJL* **913**, L29 (2021), arXiv:2103.10447 [astro-ph.HE].

[31] S. Banerjee, *Phys. Rev. D* **112**, 063016 (2025), arXiv:2505.17780 [astro-ph.GA].

[32] S. Banerjee, *MNRAS* **500**, 3002 (2021), arXiv:2004.07382 [astro-ph.HE].

[33] S. Banerjee, *A&A* **665**, A20 (2022), arXiv:2109.14612 [astro-ph.HE].

[34] J. Barber and F. Antonini, *MNRAS* **538**, 639 (2025), arXiv:2410.03832 [astro-ph.GA].

[35] L. Wang, M. Iwasawa, K. Nitadori, and J. Makino, *MNRAS* **497**, 536 (2020), arXiv:2006.16560 [astro-ph.IM].

[36] K. Kremer, C. S. Ye, N. Z. Rui, N. C. Weatherford, S. Chatterjee, G. Fragione, C. L. Rodriguez, M. Spera, and F. A. Rasio, *ApJS* **247**, 48 (2020), arXiv:1911.00018 [astro-ph.HE].

[37] A. Askar, M. Szkudlarek, D. Gondek-Rosińska, M. Giersz, and T. Bulik, *MNRAS* **464**, L36 (2017), arXiv:1608.02520 [astro-ph.HE].

[38] M. Arca Sedda, A. W. H. Kamlah, R. Spurzem, M. Giersz, P. Berczik, S. Rastello, G. Iorio, M. Mapelli, M. Gatto, and E. K. Grebel, *MNRAS* **528**, 5119 (2024), arXiv:2307.04805 [astro-ph.GA].

[39] U. N. Di Carlo, M. Mapelli, N. Giacobbo, M. Spera, Y. Bouffanais, S. Rastello, F. Santoliquido, M. Pasquato, A. r. Ballone, A. A. Trani, S. Torniamenti, and F. Haardt, *MNRAS* **498**, 495 (2020), arXiv:2004.09525 [astro-ph.HE].

[40] S. Rastello, M. Mapelli, U. N. Di Carlo, G. Iorio, A. Ballone, N. Giacobbo, F. Santoliquido, and S. Torniamenti, *MNRAS* **507**, 3612 (2021), arXiv:2105.01669 [astro-ph.GA].

[41] F. Antonini and M. Gieles, *MNRAS* **492**, 2936 (2020), arXiv:1906.11855 [astro-ph.HE].

[42] F. Antonini and M. Gieles, *Phys. Rev. D* **102**, 123016 (2020), arXiv:2009.01861 [astro-ph.HE].

[43] K. J. Joshi, F. A. Rasio, and S. Portegies Zwart, *ApJ* **540**, 969 (2000), astro-ph/9909115.

[44] A. Hypki and M. Giersz, *MNRAS* **429**, 1221 (2013), arXiv:1207.6700.

[45] H. C. Plummer, *MNRAS* **71**, 460 (1911).

[46] D. Heggie and P. Hut, *The Gravitational Million-Body Problem: A Multidisciplinary Approach to Star Cluster Dynamics* (2003).

[47] S. von Hoerner, *ApJ* **125**, 451 (1957).

[48] S. J. Aarseth, *Gravitational N-Body Simulations*, by Sverre J. Aarseth, pp. 430. ISBN 0521432723. Cambridge, UK: Cambridge University Press, November 2003. (2003) p. 430.

[49] S. Banerjee, K. Belczynski, C. L. Fryer, P. Berczik, J. R. Hurley, R. Spurzem, and L. Wang, *A&A* **639**, A41 (2020), arXiv:1902.07718 [astro-ph.SR].

[50] J. R. Hurley, O. R. Pols, and C. A. Tout, *Monthly Notices of the Royal Astronomical Society* **315**, 543 (2000).

[51] J. R. Hurley, C. A. Tout, and O. R. Pols, *Monthly Notices of the Royal Astronomical Society* **329**, 897 (2002).

[52] S. Mikkola and K. Tanikawa, *Monthly Notices of the Royal Astronomical Society* **310**, 745 (1999).

[53] S. Mikkola and D. Merritt, *AJ* **135**, 2398 (2008), arXiv:0709.3367.

[54] C. L. Fryer, K. Belczynski, G. Wiktorowicz, M. Dominik, V. Kalogera, and D. E. Holz, *ApJ* **749**, 91 (2012), arXiv:1110.1726 [astro-ph.SR].

[55] K. Belczynski, A. Heger, W. Gladysz, A. J. Ruiter, S. Woosley, G. Wiktorowicz, H.-Y. Chen, T. Bulik, R. O'Shaughnessy, D. E. Holz, C. L. Fryer, and E. Berti, *A&A* **594**, A97 (2016), arXiv:1607.03116 [astro-ph.HE].

[56] LIGO Scientific Collaboration and Virgo Collaboration, *ApJL* **896**, L44 (2020), arXiv:2006.12611 [astro-ph.HE].

[57] The LIGO Scientific Collaboration, VIRGO Collaboration, and Kagra Collaboration, *ApJL* **970**, L34 (2024), arXiv:2404.04248 [astro-ph.HE].

[58] N. Langer, C. A. Norman, A. de Koter, J. S. Vink, M. Cantiello, and S. C. Yoon, *A&A* **475**, L19 (2007), arXiv:0708.1970 [astro-ph].

[59] S. E. Woosley, *ApJ* **836**, 244 (2017), arXiv:1608.08939 [astro-ph.HE].

[60] P. Podsiadlowski, N. Langer, A. J. T. Poelarends, S. Rappaport, A. Heger, and E. Pfahl, *The Astrophysical Journal* **612**, 1044 (2004).

[61] P. Kroupa, *MNRAS* **322**, 231 (2001), astro-ph/0009005.

[62] H. Sana and C. J. Evans, in *Active OB Stars: Structure, Evolution, Mass Loss, and Critical Limits*, IAU Symposium, Vol. 272, edited by C. Neiner, G. Wade, G. Meynet, and G. Peters (2011) pp. 474–485, arXiv:1009.4197 [astro-ph.SR].

[63] H. Sana, A. de Koter, S. E. de Mink, P. R. Dunstall, C. J. Evans, V. Hénault-Brunet, J. Maíz Apellániz, O. H. Ramírez-Agudelo, W. D. Taylor, N. R. Walborn, J. S. Clark, P. A. Crowther, A. Herrero, M. Gieles, N. Langer, D. J. Lennon, and J. S. Vink, *A&A* **550**, A107 (2013), arXiv:1209.4638 [astro-ph.SR].

[64] M. Moe and R. Di Stefano, *ApJS* **230**, 15 (2017), arXiv:1606.05347 [astro-ph.SR].

[65] A. Duquennoy and M. Mayor, *A&A* **248**, 485 (1991).

[66] L. Spitzer, *Princeton, NJ, Princeton University Press, 1987*, 191 p. (1987).

[67] S. Banerjee, *MNRAS* **473**, 909 (2018), arXiv:1707.00922 [astro-ph.HE].

[68] K. Belczynski, J. Klencki, C. E. Fields, A. Olejak, E. Berti, G. Meynet, C. L. Fryer, D. E. Holz, R. O’Shaughnessy, D. A. Brown, T. Bulik, S. C. Leung, K. Nomoto, P. Madau, R. Hirschi, E. Kaiser, S. Jones, S. Mondal, M. Chruslinska, P. Drozda, D. Gerosa, Z. Doctor, M. Giersz, S. Ekstrom, C. Georgy, A. Askar, V. Baibhav, D. Wysocki, T. Natan, W. M. Farr, G. Wiktorowicz, M. Coleman Miller, B. Farr, and J. P. Lasota, *A&A* **636**, A104 (2020), arXiv:1706.07053 [astro-ph.HE].

[69] H. C. Spruit, *A&A* **381**, 923 (2002), astro-ph/0108207.

[70] J. Fuller and L. Ma, *ApJL* **881**, L1 (2019), arXiv:1907.03714 [astro-ph.SR].

[71] K. S. Thorne and A. N. Zytkow, *ApJL* **199**, L19 (1975).

[72] E. Gaburov, J. C. Lombardi, and S. Portegies Zwart, *MNRAS* **383**, L5 (2008), arXiv:0707.3021 [astro-ph].

[73] E. Glebbeek, E. Gaburov, S. E. de Mink, O. R. Pols, and S. F. Portegies Zwart, *A&A* **497**, 255 (2009), arXiv:0902.1753 [astro-ph.SR].

[74] R. Abbott, T. D. Abbott, S. Abraham, F. Acernese, K. Ackley, C. Adams, R. X. Adhikari, V. B. Adya, and et al. (LIGO Scientific Collaboration and Virgo Collaboration), *Phys. Rev. Lett.* **125**, 101102 (2020).

[75] R. Abbott, T. D. Abbott, F. Acernese, K. Ackley, C. Adams, N. Adhikari, R. X. Adhikari, V. B. Adya, and et al., *Physical Review X* **13**, 011048 (2023), arXiv:2111.03634 [astro-ph.HE].

[76] M. Gatto, V. Ripepi, M. Bellazzini, M. Tosi, M. Cignoni, C. Tortora, S. Leccia, G. Clementini, E. K. Grebel, G. Longo, M. Marconi, and I. Musella, *MNRAS* **507**, 3312 (2021), arXiv:2108.02791 [astro-ph.GA].

[77] M. Hénon, in *Dynamics of the Solar Systems*, IAU Symposium, Vol. 69, edited by A. Hayli (1975) p. 133.

[78] P. G. Breen and D. C. Heggie, *Monthly Notices of the Royal Astronomical Society* **432**, 2779 (2013).

[79] D. C. Heggie and M. Giersz, *MNRAS* **439**, 2459 (2014), arXiv:1401.3657 [astro-ph.GA].

[80] M. Spera, M. Mapelli, N. Giacobbo, A. A. Trani, A. Bressan, and G. Costa, *MNRAS* **485**, 889 (2019), arXiv:1809.04605 [astro-ph.HE].

[81] E. González, K. Kremer, S. Chatterjee, G. Fragione, C. L. Rodriguez, N. C. Weatherford, C. S. Ye, and F. A. Rasio, *ApJL* **908**, L29 (2021), arXiv:2012.10497 [astro-ph.HE].

[82] U. N. Di Carlo, M. Mapelli, Y. Bouffanais, N. Giacobbo, F. Santoliquido, A. Bressan, M. Spera, and F. Haardt, *MNRAS* **497**, 1043 (2020), arXiv:1911.01434 [astro-ph.HE].

[83] A. Ballone, G. Costa, M. Mapelli, M. MacLeod, S. Torniamenti, and J. M. Pacheco-Arias, *MNRAS* **519**, 5191 (2023), arXiv:2204.03493 [astro-ph.SR].

[84] K. Belczynski, *ApJL* **905**, L15 (2020), arXiv:2009.13526 [astro-ph.HE].

[85] J. Ziegler and K. Freese, *Phys. Rev. D* **104**, 043015 (2021), arXiv:2010.00254 [astro-ph.HE].

[86] J. S. Vink, E. R. Higgins, A. A. C. Sander, and G. N. Sabhahit, *MNRAS* **504**, 146 (2021), arXiv:2010.11730 [astro-ph.HE].

[87] L. A. C. van Son, S. E. De Mink, F. S. Broekgaarden, M. Renzo, S. Justham, E. Laplace, J. Morán-Fraile, D. D. Hendriks, and R. Farmer, *ApJ* **897**, 100 (2020), arXiv:2004.05187 [astro-ph.HE].

[88] S. Banerjee, *MNRAS* **481**, 5123 (2018), arXiv:1805.06466 [astro-ph.HE].

[89] D. Marín Pina and M. Gieles, *MNRAS* **527**, 8369 (2024), arXiv:2308.10318 [astro-ph.GA].

[90] P. C. Peters, *Physical Review* **136**, 1224 (1964).

[91] C. L. Rodriguez, P. Amaro-Seoane, S. Chatterjee, and F. A. Rasio, *Phys. Rev. Lett.* **120**, 151101 (2018).

[92] A. Mai, K. Kremer, and F. Kiroglu, *arXiv e-prints*, arXiv:2510.21916 (2025), arXiv:2510.21916 [astro-ph.GA].

[93] D. Chattopadhyay, J. Stegmann, F. Antonini, J. Barber, and I. M. Romero-Shaw, *MNRAS* **526**, 4908 (2023), arXiv:2308.10884 [astro-ph.HE].

[94] M. Arca sedda, A. W. H. Kamlah, R. Spurzem, F. P. Rizzato, M. Giersz, T. Naab, and P. Berczik, *MNRAS* **528**, 5140 (2024), arXiv:2307.04807 [astro-ph.HE].

[95] L. Paiella, C. Ugolini, M. Spera, M. Branchesi, and M. Arca Sedda, *ApJL* **994**, L54 (2025).

[96] K. Moody and S. Sigurdsson, *ApJ* **690**, 1370 (2009), arXiv:0809.1617 [astro-ph].

[97] S. Chatterjee, C. L. Rodriguez, V. Kalogera, and F. A. Rasio, *ApJL* **836**, L26 (2017), arXiv:1609.06689.

[98] A. G. Abac, I. Abouelfettouh, F. Acernese, K. Ackley, C. Adamcewicz, S. Adhikary, D. Adhikari, N. Adhikari, and et al., *ApJL* **993**, L25 (2025), arXiv:2507.08219 [astro-ph.HE].

[99] A. Borchers, C. S. Ye, and M. Fishbach, *ApJ* **987**, 146 (2025), arXiv:2503.21278 [astro-ph.HE].

[100] F. Kiroglu, K. Kremer, and F. A. Rasio, *arXiv e-prints*, arXiv:2509.05415 (2025), arXiv:2509.05415 [astro-ph.HE].

[101] J. Stegmann, A. Olejak, and S. E. de Mink, *ApJL* **992**, L26 (2025), arXiv:2507.15967 [astro-ph.HE].

[102] The LIGO Scientific Collaboration, the Virgo Collaboration, the KAGRA Collaboration, A. G. Abac, I. Abouelfettouh, F. Acernese, K. Ackley, C. Adamcewicz, S. Adhikary, D. Adhikari, N. Adhikari, and et al., *The Astrophysical Journal Letters* **993**, L21 (2025).

[103] P. Ajith, M. Hannam, S. Husa, Y. Chen, B. Brügmann, N. Dorband, D. Müller, F. Ohme, D. Pollney, C. Reisswig, L. Santamaría, and J. Seiler, *Phys. Rev. Lett.* **106**, 241101 (2011).

[104] H. Yu, S. Ma, M. Giesler, and Y. Chen, *Phys. Rev. D* **102**, 123009 (2020), arXiv:2007.12978 [gr-qc].

[105] D. Gerosa, M. Mould, D. Gangardt, P. Schmidt, G. Pratten, and L. M. Thomas, *Phys. Rev. D* **103**, 064067 (2021).

[106] S. Banerjee, A. Olejak, and K. Belczynski, *ApJ* **953**, 80 (2023), arXiv:2302.10851 [astro-ph.HE].

[107] J. Samsing and K. Hotokezaka, *ApJ* **923**, 126 (2021), arXiv:2006.09744 [astro-ph.HE].

[108] M. Bailes, B. K. Berger, P. R. Brady, M. Branchesi, K. Danzmann, M. Evans, K. Holley-Bockelmann, B. R. Iyer, and et.al., *Nature Reviews Physics* **3**, 344 (2021).

[109] P. Madau and T. Fragos, *ApJ* **840**, 39 (2017), arXiv:1606.07887 [astro-ph.GA].

[110] I. Kotko, S. Banerjee, and K. Belczynski, *MNRAS* **535**, 3577 (2024), arXiv:2403.13579 [astro-ph.SR].

[111] U. Niccolò Di Carlo, P. Agrawal, C. L. Rodriguez, and K. Breivik, arXiv e-prints , arXiv:2306.13121 (2023), arXiv:2306.13121 [astro-ph.GA].

[112] D. Marín Pina, S. Rastello, M. Gieles, K. Kremer, L. Fitzgerald, and B. Rando Forastier, *A&A* **688**, L2 (2024), arXiv:2404.13036 [astro-ph.GA].

[113] S. Chakrabarti, J. D. Simon, P. A. Craig, H. Reggiani, T. D. Brandt, P. Guhathakurta, P. A. Dalba, E. N. Kirby, P. Chang, D. R. Hey, A. Savino, M. Geha, and I. B. Thompson, *AJ* **166**, 6 (2023), arXiv:2210.05003 [astro-ph.GA].

[114] K. El-Badry, H.-W. Rix, E. Quataert, A. W. Howard, H. Isaacson, J. Fuller, K. Hawkins, K. Breivik, K. W. K. Wong, A. C. Rodriguez, C. Conroy, S. Shahaf, T. Mazeh, F. Arenou, K. B. Burdge, D. Bashi, S. Faigler, D. R. Weisz, R. Seeburger, S. Almada Monter, and J. Wojno, *MNRAS* **518**, 1057 (2023), arXiv:2209.06833 [astro-ph.SR].

[115] Gaia Collaboration, P. Panuzzo, T. Mazeh, F. Arenou, B. Holl, E. Caffau, A. Jorissen, C. Babusiaux, P. Gavras, and et al., *A&A* **686**, L2 (2024), arXiv:2404.10486 [astro-ph.GA].

[116] K. El-Badry, H.-W. Rix, D. W. Latham, S. Shahaf, T. Mazeh, A. Bieryla, L. A. Buchhave, R. Andrae, N. Yamaguchi, H. Isaacson, A. W. Howard, A. Savino, and I. V. Ilyin, *The Open Journal of Astrophysics* **7**, 58 (2024), arXiv:2405.00089 [astro-ph.SR].

[117] A. Schiebelbein-Zwack, L. A. C. van Son, M. Fishbach, and W. M. Farr, arXiv e-prints , arXiv:2511.07393 (2025), arXiv:2511.07393 [astro-ph.SR].

[118] P. André, J. Di Francesco, D. Ward-Thompson, S. I. Inutsuka, R. E. Pudritz, and J. E. Pineda, in *Protostars and Planets VI*, edited by H. Beuther, R. S. Klessen, C. P. Dullemond, and T. Henning (2014) pp. 27–51, arXiv:1312.6232 [astro-ph.GA].

[119] S. N. Longmore, J. M. D. Kruijssen, N. Bastian, J. Bally, J. Rathborne, L. Testi, A. Stolte, J. Dale, E. Bressert, and J. Alves, *Protostars and Planets VI* , 291 (2014), arXiv:1401.4175.

[120] M. Chruslinska and G. Nelemans, *MNRAS* **488**, 5300 (2019), arXiv:1907.11243 [astro-ph.GA].

[121] M. Chruslinska, G. Nelemans, L. Boco, and A. Lapi, *MNRAS* **508**, 4994 (2021), arXiv:2109.06187 [astro-ph.GA].

[122] P. J. E. Peebles, *Principles of Physical Cosmology* (1993).

[123] J. V. Narlikar, *An introduction to cosmology* (2002).

[124] Planck Collaboration, N. Aghanim, Y. Akrami, M. Ashdown, J. Aumont, C. Baccigalupi, M. Ballardini, A. J. Banday, R. B. Barreiro, and et al., *A&A* **641**, A6 (2020), arXiv:1807.06209 [astro-ph.CO].

[125] M. Gieles, S. S. Larsen, N. Bastian, and I. T. Stein, *A&A* **450**, 129 (2006), astro-ph/0512297.

[126] S. S. Larsen, *Astronomy and Astrophysics* **494**, 539 (2009).

[127] N. Bastian, A. Adamo, M. Gieles, E. Silva-Villa, H. J. G. L. M. Lamers, S. S. Larsen, L. J. Smith, I. S. Konstantopoulos, and E. Zackrisson, *MNRAS* **419**, 2606 (2012), arXiv:1109.6015 [astro-ph.CO].

[128] K. Belczynski, D. E. Holz, T. Bulik, and R. O’Shaughnessy, *Nature* **534**, 512 (2016), arXiv:1602.04531 [astro-ph.HE].

[129] M. Rafelski, A. M. Wolfe, J. X. Prochaska, M. Neeleman, and A. J. Mendez, *ApJ* **755**, 89 (2012), arXiv:1205.5047 [astro-ph.CO].

[130] M. Chruslinska, arXiv e-prints , arXiv:2206.10622 (2022), arXiv:2206.10622 [astro-ph.GA].

[131] K. Kremer, N. C. Weatherford, P. F. Hopkins, N. Z. Rui, and C. S. Ye, *ApJL* **993**, L34 (2025), arXiv:2510.11787 [astro-ph.GA].

[132] K. El-Badry, E. Quataert, D. R. Weisz, N. Choksi, and M. Boylan-Kolchin, *MNRAS* **482**, 4528 (2019), arXiv:1805.03652 [astro-ph.GA].

[133] S. F. Portegies Zwart and S. L. W. McMillan, *ApJL* **528**, L17 (2000), astro-ph/9910061.

[134] C. L. Rodriguez, M. Morscher, B. Patabiraman, S. Chatterjee, C.-J. Haster, and F. A. Rasio, *Phys. Rev. Lett.* **115**, 10.1103/physrevlett.115.051101 (2015).

[135] S. Banerjee, *Phys. Rev. D* **105**, 023004 (2022), arXiv:2108.04250 [astro-ph.HE].

[136] R. P. Kerr, *Phys. Rev. Lett.* **11**, 237 (1963).

[137] T. A. Callister and W. M. Farr, *Physical Review X* **14**, 021005 (2024), arXiv:2302.07289 [astro-ph.HE].

[138] Y. Qin, T. Fragos, G. Meynet, J. Andrews, M. Sørensen, and H. F. Song, *A&A* **616**, A28 (2018), arXiv:1802.05738 [astro-ph.SR].

[139] S. S. Bavera, T. Fragos, Y. Qin, E. Zapartas, C. J. Neijssel, I. Mandel, A. Batta, S. M. Gaebel, C. Kimball, and S. Stevenson, *A&A* **635**, A97 (2020), arXiv:1906.12257 [astro-ph.HE].

[140] Y. Qin, P. Marchant, T. Fragos, G. Meynet, and V. Kalogera, *ApJL* **870**, L18 (2019), arXiv:1810.13016 [astro-ph.SR].

[141] F. Kiroğlu, J. C. Lombardi, K. Kremer, H. D. Vanderzen, and F. A. Rasio, *ApJL* **983**, L9 (2025), arXiv:2501.09068 [astro-ph.HE].

[142] J. G. Baker, W. D. Boggs, J. Centrella, B. J. Kelly, S. T. McWilliams, M. C. Miller, and J. R. van Meter, *ApJL* **682**, L29 (2008), arXiv:0802.0416 [astro-ph].

[143] F. Hofmann, E. Barausse, and L. Rezzolla, *ApJL* **825**, L19 (2016), arXiv:1605.01938 [gr-qc].

[144] X. Jiménez-Forteza, D. Keitel, S. Husa, M. Hannam, S. Khan, and M. Pürrer, *Phys. Rev. D* **95**, 064024 (2017).

[145] C. O. Lousto, Y. Zlochower, M. Dotti, and M. Volonteri, *Phys. Rev. D* **85**, 084015 (2012), arXiv:1201.1923 [gr-qc].

[146] E. Berti and M. Volonteri, *ApJ* **684**, 822 (2008), arXiv:0802.0025 [astro-ph].

[147] A. Perego, M. Dotti, M. Colpi, and M. Volonteri, *MNRAS* **399**, 2249 (2009), arXiv:0907.3742 [astro-ph.CO].

[148] E. Cenci, L. Sala, A. Lupi, P. R. Capelo, and M. Dotti, *MNRAS* **500**, 3719 (2021), arXiv:2011.06596 [astro-ph.GA].

[149] S. Banerjee and A. Olejak, arXiv e-prints , arXiv:2411.15112 (2024), arXiv:2411.15112 [astro-ph.HE].

[150] N. Ivanova, S. Justham, X. Chen, O. De Marco, C. L. Fryer, E. Gaburov, H. Ge, E. Glebbeek, Z. Han, X. D. Li, G. Lu, T. Marsh, P. Podsiadlowski, A. Potter, N. Soker, R. Taam, T. M. Tauris, E. P. J. van den Heuvel, and R. F. Webbink, *A&A Rev.* **21**, 59 (2013), arXiv:1209.4302 [astro-ph.HE].

[151] A. A. Trani, A. Tanikawa, M. S. Fujii, N. W. C. Leigh, and J. Kumamoto, *MNRAS* **504**, 910 (2021), arXiv:2102.01689 [astro-ph.HE].

## Appendix A: Computed model clusters

TABLE III: Summary of the evolutionary star cluster model grid computed in this work and their GR-merger outcomes. All the 90 models are evolved with the direct N-body integration code **NBODY7** (Sec. II B). The model clusters initiate their evolution with a Plummer profile of total mass  $M_{\text{cl}}(0)$  and half-mass radius  $r_h(0)$ . The initial models have a primordial binary fraction of 100% for stars with zero age main sequence mass of  $m_{\text{ZAMS}} \geq 16M_{\odot}$ . For the rest of the members, an initial primordial binary fraction of 10% is adopted. All clusters orbit in a solar-neighbourhood-like external field. See Sec. II B for further details on initial conditions. The columns from left to right quote, for each model cluster, the initial mass,  $M_{\text{cl}}(0)$ , initial membership,  $N(0)$ , initial half-mass radius,  $r_h(0)$ , metallicity,  $Z$ , maximum number of bound BH members during cluster evolution,  $N_{\text{BH,max}}$ , end time of the simulation,  $t_{\text{end}}$ , total membership at the end of the simulation,  $N_{\text{end}}$ , BH membership at the end of the simulation,  $N_{\text{BH,end}}$ , number of in-cluster mergers,  $N_{\text{mrg,in}}$ , and number of ejected mergers,  $N_{\text{mrg,esc}}$ .

Model nr.	$M_{\text{cl}}(0)[M_{\odot}]$	$N(0)$	$r_h(0)[\text{pc}]$	$Z$	$N_{\text{BH,max}}$	$t_{\text{end}}[\text{Gyr}]$	$N_{\text{end}}$	$N_{\text{BH,end}}$	$N_{\text{mrg,in}}$	$N_{\text{mrg,esc}}$
1	10000.0	17329	1.0	0.0002	12	3.0	8290	0	0	0
2	10000.0	17329	1.0	0.0010	16	9.7	51	0	1	0
3	10000.0	17329	1.0	0.0050	12	1.0	14510	0	0	1
4	10000.0	17329	1.0	0.0100	10	1.0	14408	0	1	0
5	10000.0	17329	1.0	0.0200	6	5.6	1357	0	0	0
6	10000.0	17329	2.0	0.0002	18	9.2	96	0	0	0
7	10000.0	17329	2.0	0.0010	11	7.7	52	0	0	0
8	10000.0	17329	2.0	0.0050	10	7.8	492	0	0	0
9	10000.0	17329	2.0	0.0100	10	6.3	53	2	1	0
10	10000.0	17329	2.0	0.0200	5	5.3	2345	0	0	0
11	10000.0	17329	3.0	0.0002	17	3.2	55	0	0	0
12	10000.0	17329	3.0	0.0010	15	6.1	57	0	0	0
13	10000.0	17329	3.0	0.0050	9	8.9	51	0	1	0
14	10000.0	17329	3.0	0.0100	11	6.9	2	0	0	0
15	10000.0	17329	3.0	0.0200	5	7.3	554	0	0	0
16	20000.1	34425	1.0	0.0002	35	11.0	1783	0	1	0
17	20000.1	34426	1.0	0.0010	26	1.7	27936	2	0	0
18	20000.1	34426	1.0	0.0050	28	0.7	32000	2	0	0
19	20000.1	34424	1.0	0.0100	18	1.3	29860	0	2	0
20	20000.1	34426	1.0	0.0200	12	3.6	18702	0	0	0
21	20000.1	34426	2.0	0.0002	30	7.9	8810	1	1	0
22	20000.1	34426	2.0	0.0010	28	9.9	4697	0	0	1
23	20000.1	34425	2.0	0.0050	30	5.8	14157	1	1	0
24	20000.1	34426	2.0	0.0100	20	7.1	10313	0	0	0
25	20000.1	34426	2.0	0.0200	9	7.0	8091	0	0	0
26	20000.1	34426	3.0	0.0002	31	11.0	1626	1	0	0
27	20000.1	34426	3.0	0.0010	28	8.2	61	0	1	1

Continued on next page

Model nr.	$M_{\text{cl}}(0)[M_{\odot}]$	$N(0)$	$r_h(0)[\text{pc}]$	$Z$	$N_{\text{BH,max}}$	$t_{\text{end}}[\text{Gyr}]$	$N_{\text{end}}$	$N_{\text{BH,end}}$	$N_{\text{mrg,in}}$	$N_{\text{mrg,esc}}$
28	20000.1	34426	3.0	0.0050	25	11.0	754	2	2	0
29	20000.1	34425	3.0	0.0100	17	11.0	2631	0	1	0
30	20000.1	34426	3.0	0.0200	12	6.2	10933	0	0	0
31	30000.1	51509	1.0	0.0002	48	2.9	40723	1	0	1
32	30000.1	51509	1.0	0.0010	44	11.0	11703	2	1	0
33	30000.1	51509	1.0	0.0050	38	5.5	28333	0	1	0
34	30000.1	51509	1.0	0.0100	31	2.5	41210	0	0	0
35	30000.1	51509	1.0	0.0200	18	1.0	48273	2	0	0
36	30000.1	51509	2.0	0.0002	48	10.3	13886	0	2	0
37	30000.1	51509	2.0	0.0010	42	11.0	12727	2	2	0
38	30000.1	51509	2.0	0.0050	31	11.0	11933	0	1	0
39	30000.1	51509	2.0	0.0100	27	11.0	12164	0	2	0
40	30000.1	51509	2.0	0.0200	16	9.2	14111	0	0	0
41	30000.1	51508	3.0	0.0002	45	11.0	7501	2	0	0
42	30000.1	51508	3.0	0.0010	41	11.0	7837	0	1	0
43	30000.1	51508	3.0	0.0050	38	10.1	14168	2	0	0
44	30000.1	51508	3.0	0.0100	32	11.0	11457	2	0	0
45	30000.1	51508	3.0	0.0200	18	10.7	10637	0	0	0
46	50000.0	85661	1.0	0.0002	77	7.9	51743	0	3	0
47	50000.0	85660	1.0	0.0010	69	5.6	61924	0	1	1
48	50000.0	85662	1.0	0.0050	66	4.0	68446	0	0	0
49	50000.0	85662	1.0	0.0100	52	3.6	69981	1	3	0
50	50000.0	85662	1.0	0.0200	32	1.9	77665	0	2	0
51	50000.0	85662	2.0	0.0002	76	11.0	38615	0	0	0
52	50000.0	85662	2.0	0.0010	77	11.0	39803	2	1	0
53	50000.0	85662	2.0	0.0050	65	9.3	47519	0	3	1
54	50000.0	85662	2.0	0.0100	53	6.5	60200	0	0	0
55	50000.0	85662	2.0	0.0200	41	2.9	75480	3	0	0
56	50000.0	85662	3.0	0.0002	80	11.0	34963	3	0	0
57	50000.0	85662	3.0	0.0010	75	11.0	36463	5	0	0
58	50000.0	85662	3.0	0.0050	63	11.0	38416	1	1	0
59	50000.0	85662	3.0	0.0100	60	11.0	38961	0	0	0
60	50000.0	85662	3.0	0.0200	30	11.0	38037	0	1	0
61	75000.0	128343	1.0	0.0002	124	5.4	104244	0	4	3
62	75000.0	128343	1.0	0.0010	109	5.4	103420	0	4	3
63	75000.0	128343	1.0	0.0050	109	4.0	110207	2	5	2
64	75000.0	128343	1.0	0.0100	81	2.8	116295	0	4	0
65	75000.0	128343	1.0	0.0200	48	2.3	117970	1	0	0
66	75000.0	128343	2.0	0.0002	112	11.0	78032	4	5	1
67	75000.0	128343	2.0	0.0010	108	11.0	81463	2	3	4
68	75000.0	128343	2.0	0.0050	107	9.7	87377	1	3	1
69	75000.0	128341	2.0	0.0100	75	8.1	94562	1	1	1
70	75000.0	128343	2.0	0.0200	53	6.6	101019	0	0	0
71	75000.0	128342	3.0	0.0002	117	9.9	81921	4	2	3
72	75000.0	128343	3.0	0.0010	110	11.0	76965	5	2	1
73	75000.0	128343	3.0	0.0050	106	9.7	84644	5	1	2

Continued on next page

Model nr.	$M_{\text{cl}}(0)[M_{\odot}]$	$N(0)$	$r_h(0)[\text{pc}]$	$Z$	$N_{\text{BH,max}}$	$t_{\text{end}}[\text{Gyr}]$	$N_{\text{end}}$	$N_{\text{BH,end}}$	$N_{\text{mrg,in}}$	$N_{\text{mrg,esc}}$
74	75000.0	128343	3.0	0.0100	88	7.7	94552	3	2	0
75	75000.0	128343	3.0	0.0200	49	11.0	78319	2	1	0
76	100000.1	171019	1.0	0.0002	162	3.3	155252	8	4	1
77	100000.1	171019	1.0	0.0010	160	2.7	158083	22	2	1
78	100000.1	171017	1.0	0.0050	126	3.4	155810	2	3	3
79	100000.1	171019	1.0	0.0100	117	4.1	151359	0	3	1
80	100000.1	171018	1.0	0.0200	73	2.8	157772	0	0	0
81	100000.1	171018	2.0	0.0002	166	10.4	125080	4	4	3
82	100000.1	171018	2.0	0.0010	156	11.0	119026	7	4	1
83	100000.1	171019	2.0	0.0050	131	7.5	139780	2	6	0
84	100000.1	171019	2.0	0.0100	117	3.5	157352	8	1	1
85	100000.1	171019	2.0	0.0200	76	0.7	167527	23	0	1
86	100000.1	171019	3.0	0.0002	162	10.7	114885	13	4	1
87	100000.1	171019	3.0	0.0010	147	10.1	120540	15	2	1
88	100000.1	171017	3.0	0.0050	137	10.3	123356	3	1	1
89	100000.1	171019	3.0	0.0100	116	4.8	149719	20	1	0
90	100000.1	171019	3.0	0.0200	78	10.9	122221	2	3	0

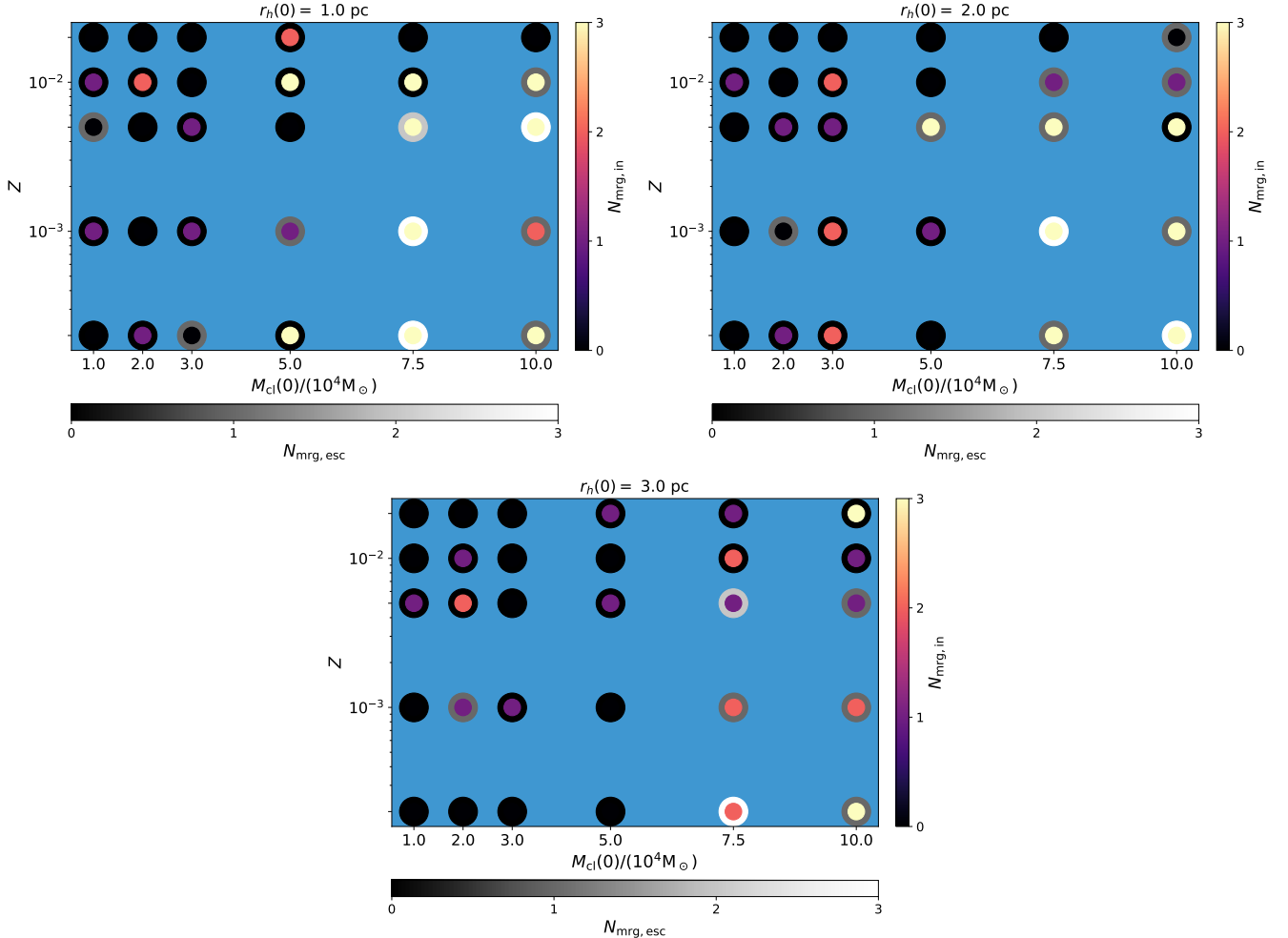


FIG. 14. Analogous description as in Fig. 1 applies. Here, the fill colour represents the number of GW mergers inside the corresponding computed cluster and the edge colour represents the number of mergers (within a Hubble time) among the compact binaries that escape the cluster.

## Appendix B: Merger rate density from model merger population

To obtain the redshift-dependent merger rate density from YMC/OC, a Model Universe is constructed out of the computed evolutionary model grid. The intrinsic merger rate density,  $\mathcal{R}(z)$ , at a redshift  $z$  can be formally expressed as

$$\mathcal{R}(z) = \frac{n_{\text{cl}}}{\Delta t_{\text{age}}(\Delta z(z))} \int_{z_f,u}^{z_f=z} \int_{Z=Z_1}^{Z_u} \int_{M_{\text{cl}}=M_{\text{cl},1}}^{M_{\text{cl},u}} \int_{r_h=r_{h,1}}^{r_{h,u}} \mathcal{F}_{\text{mrg}}(z, z_f, M_{\text{cl}}, r_h, Z) \phi_{\text{CLMF}}(M_{\text{cl}}) \phi_r(r_h) \phi_{Z,Z}(z_f, Z) \phi_{\text{SFH}}(z_f) dr_h dM_{\text{cl}} dZ dz_f \quad (B1)$$

Here, the functions  $\phi_{\text{CLMF}}(M_{\text{cl}})$ ,  $\phi_r(r_h)$ ,  $\phi_{Z,Z}(z_f, Z)$ ,  $\phi_{\text{SFH}}(z_f)$  are, respectively, the probability distribution of a star cluster's initial mass,  $M_{\text{cl}}$ , initial size,  $r_h$ <sup>9</sup>, metallicity,  $Z$ , and formation redshift,  $z_f$ , in the Universe. The function  $\mathcal{F}_{\text{mrg}}(z, z_f, M_{\text{cl}}, r_h, Z)$  is the number of GR mergers that a cluster, formed at a redshift  $z_f$  with parameters  $M_{\text{cl}}$ ,  $r_h$ , and  $Z$ , produces at the redshift  $z$ . That way,  $\mathcal{F}_{\text{mrg}}$  allows for taking the mergers' delay time,  $t_{\text{mrg}}$ , into account: in

<sup>9</sup> For the convenience of notation, in this subsection, the initial mass and size of a cluster are denoted by  $M_{\text{cl}}$  and  $r_h$ , respectively,

instead of  $M_{\text{cl}}(0)$  and  $r_h(0)$  as used in other places in this paper.

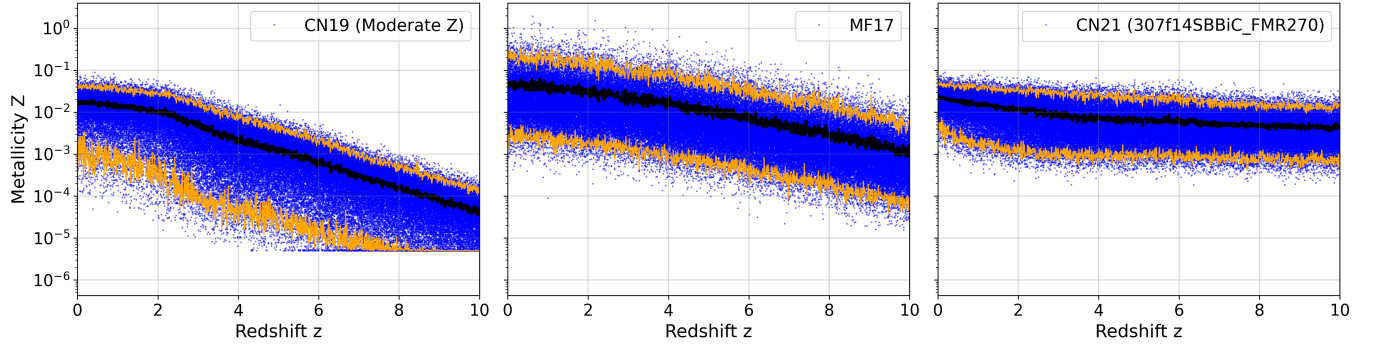


FIG. 15. Redshift ( $z$ ) - metallicity ( $Z$ ) or  $zZ$  sample as of Ref. [109] (MF17; middle panel), Ref. [120] (CN19; left panel), and Ref. [121] (CN21; right panel). For the case of MF17  $zZ$  dependence, a spread in metallicity of 0.5 dex is assumed. For the case of CN19  $zZ$  dependence, the variant ‘Moderate-Z’ is chosen. For the case of CN21  $zZ$  dependence, the variant 307f14SBBiC\_FMR270 is chosen. On each panel, the black line traces the mean and the orange lines enclose the 95% CI of the  $Z$ -distribution at increasing  $z$ .

this function,  $z = \mathcal{Z}(\mathcal{Z}^{-1}(z_f) + t_{\text{mrg}})$ , where the function  $\mathcal{Z}(t_{\text{age}})$  converts the age of the Universe,  $t_{\text{age}}$ , into redshift. In this study, the age-redshift relation corresponding to the standard  $\Lambda$ CDM cosmological framework [122, 123] is adopted, where the cosmological constants from the Planck mission [124] (Hubble constant  $H_0 = 67.4 \text{ km s}^{-1} \text{ Mpc}^{-1}$ , matter content  $\Omega_m = 0.315$ , flat Universe, for which  $t_{\text{Hubble}} = 13.79 \text{ Gyr}$ ) are applied. Note that  $\mathcal{F}_{\text{mrg}}$  effectively encodes the merger efficiency  $\eta_{\text{mrg}}$ .

The quantity  $n_{\text{cl}}$  is the number of star clusters formed per unit comoving volume. The quantity  $\Delta t_{\text{age}}(\Delta z(z))$  is the age range (or age bin) of the Universe corresponding to the redshift bin  $\Delta z(z)$  around the redshift of interest  $z$ . As for the integral limits,  $X_l$  and  $X_u$  represent the lower and upper limits of the integration variable  $X$ .

In practice, due to the discrete model grid points and a limited number of mergers (155 of them) from them, a Monte-Carlo approach is adopted to tackle the multi-dimensional integral in Eqn. B1. Here,  $N_{\text{samp}}$  star clusters are randomly selected such that

$$M_{\text{cl}} \in \phi_{\text{CLMF}}(M_{\text{cl}}) \propto M_{\text{cl}}^{-2} \quad 10^4 M_{\odot} \leq M_{\text{cl}} \leq 10^5 M_{\odot}, \quad (\text{B2})$$

$$r_h \in \mathcal{U}(0, 1)(r_{h,u} - r_{h,l}) + r_{h,l} \quad r_{h,l} = 1 \text{ pc}, \quad r_{h,u} = 3 \text{ pc}, \quad (\text{B3})$$

where  $\mathcal{U}(0, 1)$  is the uniform distribution over  $[0, 1]$ . The  $M_{\text{cl}}^{-2}$  dependence is supported by observations of young clusters in the Milky Way and nearby galaxies [23, 125–127]. The formation redshift is chosen such that

$$z_f \in \phi_{\text{SFH}}(z_f) \propto \frac{(1 + z_f)^{2.6}}{1 + [(1 + z_f)/3.2]^{6.2}}, \quad (\text{B4})$$

which is the redshift dependence of star formation rate density as of Ref. [109].

As for the redshift-dependent metallicity distribution, a variety of observation-based  $zZ$  dependence,  $\phi(zZ)$ , have been proposed. A commonly used relation that is considered here is the observation-based algebraic redshift-metallicity relation of Ref. [109] superimposed with a log-normal scatter in metallicity of 0.5 dex (as in, *e.g.*, Refs. [97, 128]), *i.e.*,

$$\log_{10}(Z(z)/Z_{\odot}) \in \mathcal{N}(\mu = 0.153 - 0.074z^{1.34}, \sigma = 0.5), \quad (\text{B5})$$

where  $\mathcal{N}(\mu, \sigma)$  is the normal distribution with mean  $\mu$  and dispersion  $\sigma$ . The above spread in  $Z$  is based on observations of damped Ly $\alpha$  systems up to high redshifts [129]. This  $zZ$  dependence is termed MF17 in this study.

Due to the importance of cosmic metallicity evolution on GW source formation and GW astrophysics (see Ref. [130] for a review), more recent, observation-based  $zZ$  dependences of Refs. [120] and [121] are also considered in this study. These latter  $zZ$  dependences explicitly provide observationally derived metallicity scatter in star forming regions up to redshift 10. Among the wide variety of  $\phi_{zZ}(z, Z)$  provided in those works, the variants Moderate-Z (hereafter CN19) from Ref. [120] and 307f14SBBiC\_FMR270 (hereafter CN21) from Ref. [121] are considered here due to their non-extreme nature and the inclusion of the latest observations. Sample draws from these three  $\phi_{zZ}(z, Z)$  schemes are shown in Fig. 15<sup>10</sup>. As seen in Fig. 15, the metallicity declines with increasing redshift in all three cases. However,

<sup>10</sup> These  $zZ$  samples are generated utilising the scripts provided in

Refs. [120, 121].

the CN19, MF17, and CN21 schemes produce, in order, increasingly higher mean metallicity and smaller scatter in metallicity. That way, these choices allow for some leeway to explore potential variations in the redshift-metallicity dependence, consistently with high-redshift observations. Since all the above  $zZ$ -schemes incorporate observations beginning from the local Universe up to redshift 10, the lower and upper limits of the cluster-formation redshift are set to be  $z_{f,l} = 0$  and  $z_{f,u} = 10$ .

After each random draw of a star cluster's initial and formation parameters from the various distributions as described above, the parameters  $M_{\text{cl}}$ ,  $r_h$ , and  $Z$  are discretised based on the available grid points (Sec. II A, Figs. 1 & 14), and the GW coalescences (if any) from the corresponding model cluster are individually mapped at the appropriate redshifts based on the events'  $t_{\text{mrg}}$ , the cluster's  $z_f$ , and the background cosmological model (see above). The redshift-dependent intrinsic merger rate density is then given by

$$\mathcal{R}(z) \approx \left( \frac{\Delta N_{\text{mrg}}(\Delta z(z))}{N_{\text{samp}}} \right) \left( \frac{1}{\Delta t_{\text{age}}(\Delta z(z))} \right) \left[ \frac{\int_{M_{\text{cl},l}}^{M_{\text{cl},u}} \phi_{\text{CLMF}}(M_{\text{cl}}) dM_{\text{cl}}}{\int_{M_{\text{GC},l}}^{M_{\text{GC},u}} \phi_{\text{CLMF}}(M_{\text{cl}}) dM_{\text{cl}}} \right] \left[ \frac{\int_{10}^0 \phi_{\text{SFH}}(z_f) dz_f}{\int_6^3 \phi_{\text{SFH}}(z_f) dz_f} \right] n_{\text{GC}}, \quad (\text{B6})$$

where  $\Delta N_{\text{mrg}}(\Delta z(z))$  is the number of events contained within the redshift bin  $\Delta z(z)$ . The quantity  $n_{\text{GC}}$  is the comoving spatial number density of GCs, with respect to which  $n_{\text{cl}}$  in Eqn. B1 is scaled. In Eqn. B6, this scaling is done in the same way as in Ref. [29] (see their Eqn. 5). To summarise,  $n_{\text{GC}}$  is boosted to  $n_{\text{cl}}$  due to (a) newly formed star clusters extending to lower masses than the GCs and (b) cluster formation across masses extending up to the present day, as opposed to the present-day GCs that are old objects.

Due to the mass range of the model clusters with which the Model Universe is populated,  $[M_{\text{cl},l}, M_{\text{cl},u}] = [10^4 M_{\odot}, 10^5 M_{\odot}]$  is set in Eqn. B6. As in Ref. [29], the birth mass range of GCs,  $[M_{\text{GC},l}, M_{\text{GC},u}]$ , is chosen based on the initial masses of the GC models in the CMC Cluster Catalog [36] (hereafter CCC), which models reasonably represent the observed present-day Milky Way GC population [26, 131]. In CCC, the typical present-day GC masses were obtained by evolving from initial masses within  $[M_{\text{GC},l}, M_{\text{GC},u}] = [5 \times 10^5 M_{\odot}, 1 \times 10^6 M_{\odot}]$ , which mass range is taken here for evaluating a ‘reference’  $\mathcal{R}(z)$  from Eqn. B6. The entire Milky Way GC mass range (*i.e.*, including the least and most massive GCs) was obtained from  $[M_{\text{GC},l}, M_{\text{GC},u}] = [1 \times 10^5 M_{\odot}, 2 \times 10^6 M_{\odot}]$ , which mass range is used here for obtaining a ‘pessimistic’ rate,  $\mathcal{R}_-(z)$ . The formation redshift range of GCs in the denominator of Eqn. B6 is taken to be  $3.0 \lesssim z_f \lesssim 6.0$  based on cosmological structure formation modelling [132]. As for the spatial density of GCs, the observationally determined value of  $n_{\text{GC}} \approx 8.4 h^3 \text{Mpc}^{-3} \approx 2.57 \text{Mpc}^{-3}$  [133] ( $h \equiv H_0/[100 \text{ km s}^{-1} \text{ Mpc}^{-1}] = 0.674$  [124]) is applied for obtaining the reference  $\mathcal{R}(z)$  and  $n_{\text{GC}} \approx 0.33 \text{Mpc}^{-3}$  [134] is applied for the pessimistic  $\mathcal{R}_-(z)$ . While the above approach makes the merger rate estimation independent of explicitly assuming a cluster formation efficiency, it implicitly assumes that (i) star cluster formation in the Universe follows the cosmic star formation history and (ii) star clusters are formed at all redshifts with the same universal mass distribution. See Refs. [29, 135] for detailed discussions on these choices and assumptions.

If  $p(A)|_z$  is the normalised density distribution of a GW observable,  $A$ , for the events in the redshift bin  $\Delta z(z)$ , then the differential intrinsic merger rate density with respect to  $A$  at redshift  $z$  is

$$\frac{d\mathcal{R}}{dA}(A) \Big|_z = \mathcal{R}(z) p(A)|_z \quad (\text{B7})$$

If the number of events detected within the  $i$ -th  $A$ -bin of width  $\Delta A_i$  around  $A = A_i$  is  $\Delta N_{A,i}|_z$  ( $\sum_i \Delta N_{A,i}|_z = \Delta N_{\text{mrg}}(\Delta z(z))$ ) then

$$\frac{d\mathcal{R}}{dA}(A_i) \Big|_z \approx \mathcal{R}(z) \frac{\Delta N_{A,i}|_z}{\Delta A_i \Delta N_{\text{mrg}}(\Delta z(z))}. \quad (\text{B8})$$

### Appendix C: Assigning BH spins and BBH spin-orbit tilts

During the N-body simulations performed here, dimensionless spin magnitude (or Kerr parameter [136]) is assigned runtime to all newly formed or mass-gained stellar-remnant BHs. For a BH that is derived from a single star (that either is evolved from ZAMS or is a rejuvenated star-star merger product) or from a non-interacting stellar member of a binary or higher-multiplicity system inside the cluster, a small natal spin magnitude is assigned based on hydrodynamic calculations of BH formation from single stars. In particular, the ‘MESA’ BH-spin model of Ref. [68] is adopted in the present N-body simulations, which prescription assigns a BH-spin within  $0.05 \lesssim a \lesssim 0.15$  depending on the properties of the pre-core-collapse star and the metallicity. The small BH spin is due to the dynamo-driven efficient core-to-envelope angular momentum transport [69] in the stellar evolution models computed in Ref. [68]. In fact, Ref. [70] modelled a rather extreme version of the dynamo-driven angular momentum extraction, where the BHs

were formed with nearly vanishing spin,  $a \sim 10^{-1}$ . However, the higher, standard-dynamo-based BH spin is preferred in this work since the to-date-observed GW events tend to favour small but non-zero magnitudes of  $a \sim 10^{-1}$  [17, 137].

In the current modelling, the spin magnitude of a BH can, however, be higher than this dynamo-driven value, *i.e.*, the BH can be ‘spun-up’ due to (a) tidal spin-up of the BH’s WR-star progenitor in a close, tidally interacting binary [68, 138, 139], (b) matter accretion onto the BH due to a BH-star merger and/or mass transfer from a binary companion [140, 141], (c) GW coalescence with another BH [142–144]. In the present **NBODY7** version, no recipe or algorithm is yet implemented for runtime BH spin alteration (boost) via channels (a) and (b), although these channels themselves are identified during a run. The BHs that are outcomes of channels (a) and (b) are simply tagged runtime as maximally spinning BHs, *i.e.*, with  $a = 1$ . At present, no Kerr parameter is assigned to NS members, and any GR merger involving an NS is excluded from the calculation of spin-related parameters such as  $\chi_{\text{eff}}$ . Improvements in the treatments are planned in the near future.

As for BBH mergers happening inside a model cluster (*i.e.*, channel (c)), the GR recoil kick and the final spin of the merged BH are obtained based on analytical fits to NR BBH merger calculations as of Refs. [143, 145]. The recoil velocity and final spin depend on both the BH components’ spin magnitude and direction relative to the BBH’s orbital angular momentum. Here, the spin-orbit tilt and azimuthal angles are drawn randomly from a full isotropic distribution if the merging BBH is purely dynamically assembled. A partial alignment is applied with a truncated isotropic tilt distribution if the BBH’s components were members of the same primordial binary. Notably, inside a cluster, a BH’s spin can be modified by a combination of the above channels. The reader is directed to Refs. [32, 49] for all the details and the formulae of the above implementations in the **NBODY7** code.

However, the presence of by-construction maximally spinning BH members in a population of merging BBHs can lead to artefacts in, *e.g.*, the population’s  $\chi_{\text{eff}}$  distribution. In this work, this is addressed by reassigning post-run the spins of those BHs that are outcomes of channels (a) and (b). Spin alteration of a BH via mass accretion is rather poorly understood (*e.g.*, [146–148]); hence for channel (b) the spin magnitude of the mass-accreted BH is reassigned tacitly from a uniform distribution between  $0.5 \leq a \leq 1.0$ . Ref. [18] provides indirect support to this range of spin for high-spin BHs.

Those BHs that are derived via channel (a) are mainly primordially paired, since such close, tidally interacting binaries (orbital period  $\lesssim 1$  day) would rarely undergo close dynamical encounters [46]. Therefore, BH spins and spin-orbit tilts of all the primordially paired mergers in a BBH merger population are replaced with those from a separate isolated binary population evolution calculation, where each binary is evolved independently without undergoing any dynamical encounter. For consistency, this isolated binary evolution modelling is performed with a standalone version of the same **BSE** binary evolution code that is coupled with **NBODY7** (Sec. II B). However, this version, in addition, explicitly takes into account tidal spin-up of WR progenitors while assigning spin magnitudes to newly formed BHs. Furthermore, the spin-orbit tilts are determined based on the BHs’ natal kicks. This version of **BSE** is described in detail in Ref. [149]. In particular, the spin magnitudes are determined by their Eqns. 4–6 and the tilts are given by their Eqn. 10.

The isolated binary evolution calculations are carried out with an initial massive binary population whose distributions match those of the initial (primordial) massive binary population in the N-body models computed here (Sec. II B). Some  $2 \times 10^6$  binaries are evolved for each metallicity in the N-body model grid, *i.e.*, at  $Z = 0.0002, 0.001, 0.005, 0.01, 0.02$ . Each set is evolved under identical model choices as for the N-body runs (Sec. II B), *i.e.*, delayed remnant mass model with PPSN/PSN, ‘MESA’ (non-spun-up) BH spin model, common envelope efficiency parameter  $\alpha_{\text{CE}} = 1.0$  [51, 150], **BSE**’s default binding energy parameter [51], fallback-modulated, momentum-conserving remnant natal kick scheme [49], and Eddington-limited mass accretion. The default binary mass transfer physics of **BSE** (*e.g.*, mass transfer stability criteria, angular momentum transport, super-Eddington mass transfer treatment [51]) is applied in these isolated binary evolution runs (although alternative treatments of mass transfer physics were also demonstrated in Ref. [149]), as for the N-body runs.

These isolated binary evolutionary models produce a population of merging BBHs whose members can potentially be spun-up depending on the BBH’s parent binary’s evolution history. If not spun-up, then a merging BH member possesses the appropriate dynamo-driven spin magnitude; see Ref. [149] for the details. For every primordially paired BBH merger originating from a cluster of metallicity  $Z'$ , the member BHs’ spin magnitudes and spin-orbit tilts are reassigned by picking the spin pair,  $a_1, a_2$ , and the tilt pair,  $\nu_1, \nu_2$ , of a merging BBH chosen randomly out of the isolated-binary set of metallicity  $Z'$ . That way, the reassigned spin magnitudes statistically incorporate the effect of possible tidal spin-up of BH-progenitor WR stars.

Since the formation of the BH members, a primordially paired in-cluster or ejected merging BBH would generally experience additional spin-orbit tilt (which tilt is common to both members) due to close dynamical encounters. This would make the BBH more misaligned than its isolated-binary counterpart [151]. In this study, this effect is taken into account by vector-adding a spin-orbit tilt, selected randomly from the dynamical tilt distribution of Ref. [151] (corresponding to the appropriate metallicity), to both members of a primordially paired BBH. The procedure followed for this is detailed in Ref. [106]. This reassignment is done after the first set of reassignment from the isolated-binary

models (see above). These spin and tilt reassessments are done for both the BBH merger events extracted directly from the cluster models (Sec. IV) and the Model Universe BBH events across redshifts (Appendix B).

For all in-cluster or ejected BBH mergers that are dynamically paired, an isotropic spin-orbit tilt distribution is assumed for both components independently, after reassigning the spins of the high-spin BH candidates (see above). In other words, for all dynamically paired BBH inspirals,  $(\cos \theta_1, \cos \theta_2) \in \mathcal{U}(-1, 1)$ , where  $\mathcal{U}(-1, 1)$  is the uniform distribution over  $[-1, 1]$  (Eqn. 4). This is because members of stellar entities can, in general, be taken to be uncorrelated over the length scale of a parsec-scale star cluster.

#### Appendix D: Additional illustrations

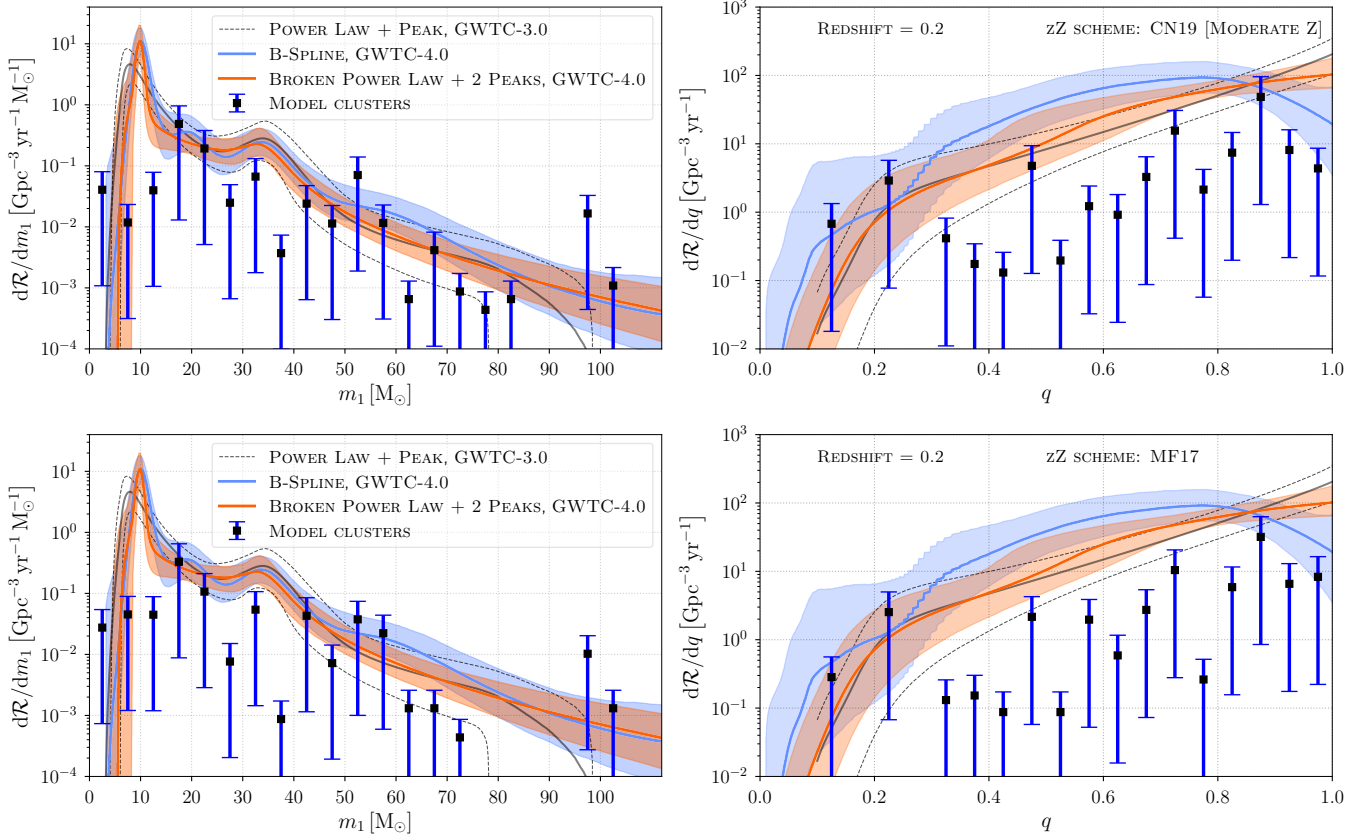


FIG. 16. Same description as in Fig. 9 applies. The model differential merger rate density distributions presented in the upper (lower) pair of panels correspond to the CN19 (MF17)  $zZ$  scheme.

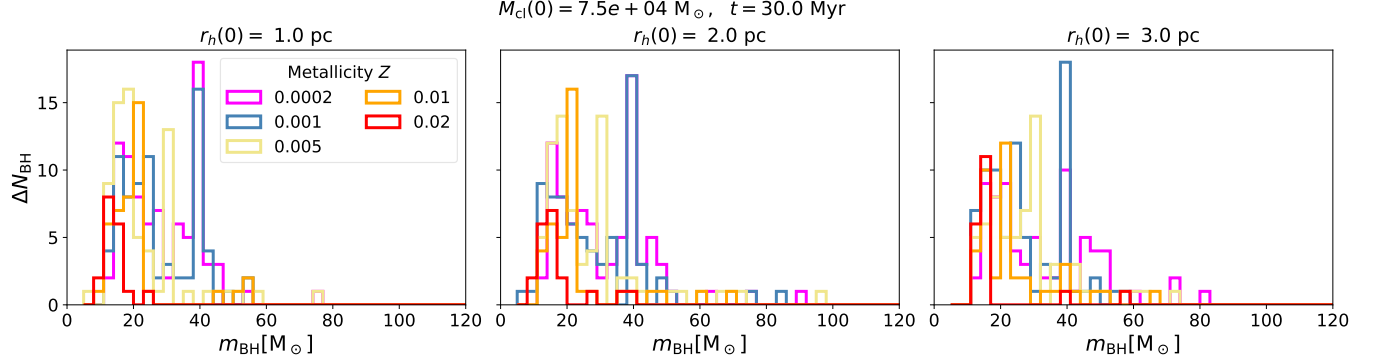


FIG. 17. Mass distribution of BHs that are retained in the cluster after formation. Here, the distributions for the  $M_{\text{cl}}(0) = 7.5 \times 10^4 M_{\odot}$  clusters are plotted. The left, middle, and right panels plot those for the  $r_h(0) = 1$  pc, 2 pc, and 3 pc model clusters, respectively, of all the five metallicities (legend). The distributions are plotted at an evolutionary time of 30 Myr, which is sufficiently beyond the time over which the BHs are formed inside the clusters (3–20 Myr) so that the unbound BHs with high natal kick have escaped from the cluster, but too early for the BHs to be dynamically active via central core formation (Sec. III A, Fig. 2). That way, the birth mass distribution of the initially cluster-retained BHs is captured. The cluster-retained ESC-NSs are excluded from this plot.

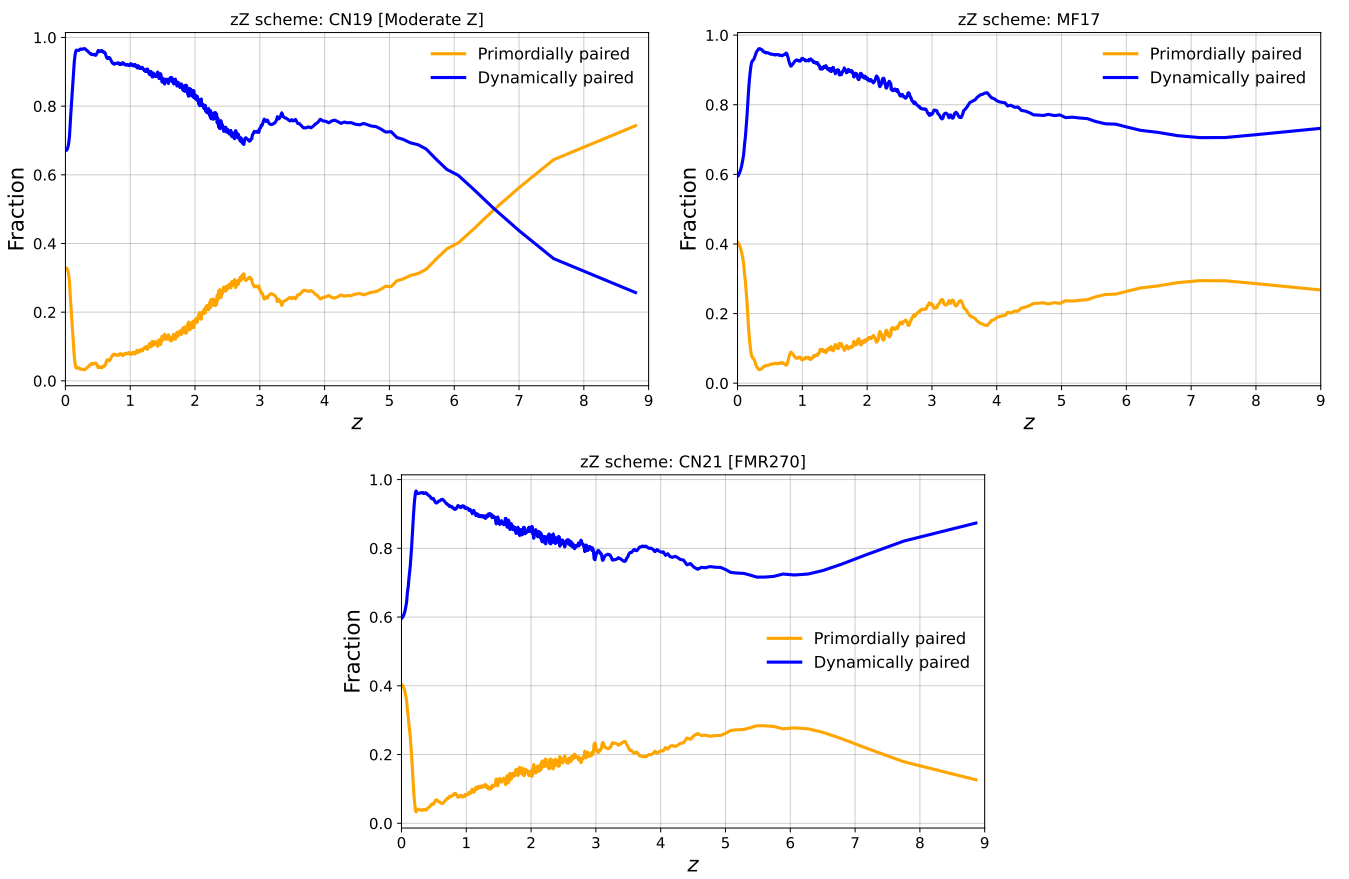


FIG. 18. Evolution of the fractions of primordially paired and dynamically paired mergers (legend) with redshift, for the model merger population syntheses performed in this work. The three panels distinguish the adopted  $zZ$  schemes, namely, MF17, CN19, and CN21 (panel subtitle).

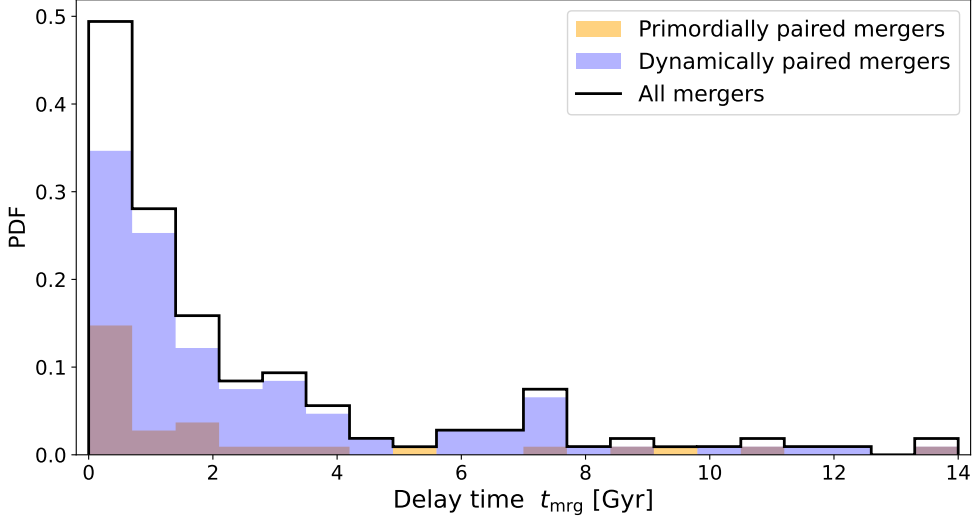


FIG. 19. Distribution (probability density function) of delay time,  $t_{\text{mrg}}$ , of the mergers from the model cluster grid, shown separately for the primordially paired and dynamically paired mergers (filled histograms) as well as for the combined merger population (empty histogram). The combined distribution is normalised to be integrated up to unity. The integrals of the primordially paired and dynamically paired distributions are scaled according to the respective sub-population's count relative to the total merger count (so that the distributions add up to the normalised combined distribution).

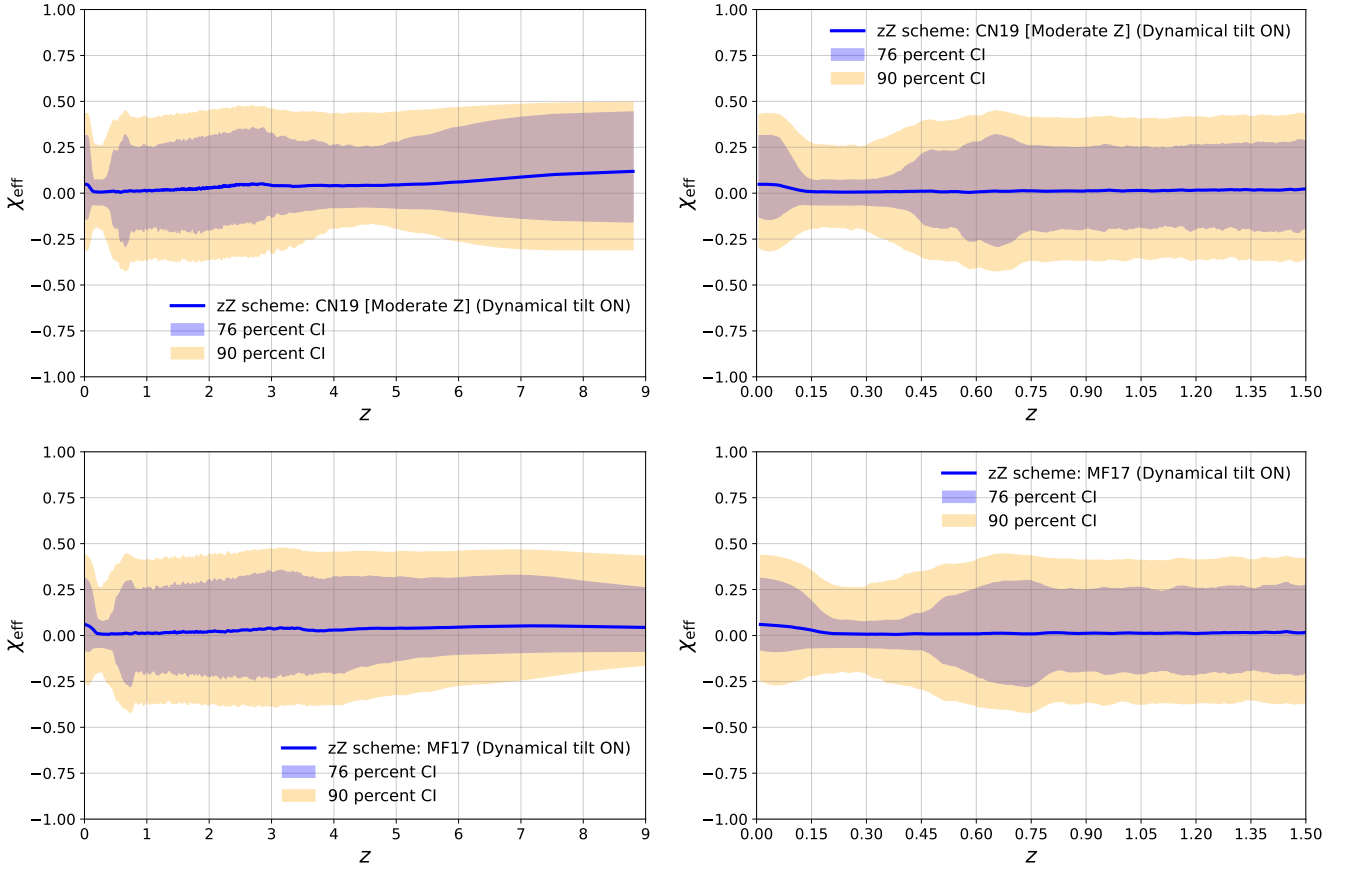


FIG. 20. Same description as in Fig. 11 applies. The model  $\chi_{\text{eff}}$  distribution evolutions presented in the upper (lower) pair of panels correspond to the CN19 (MF17)  $zZ$  scheme.